2017

Rock Magnetic Investigation of the Michigan Basin Soils and Sediments Overlying the Oil-Bearing Silurian Pinnacle Reefs

Jake Tresnak
Michigan Technological University, jptresna@mtu.edu

ROCK MAGNETIC INVESTIGATION OF THE MICHIGAN BASIN SOILS AND SEDIMENTS OVERLYING THE OIL-BEARING SILURIAN PINNACLE REEFS

By

Jacob P. Tresnak

A THESIS

Submitted in partial fulfillment of the requirements for the degree of
MASTER OF SCIENCE
In Geophysics

MICHIGAN TECHNOLOGICAL UNIVERSITY

2017

This thesis has been approved in partial fulfillment of the requirements for the Degree of MASTER OF SCIENCE in Geophysics.

Department of Geological and Mining Engineering and Sciences

Thesis Advisor: *Aleksey Smirnov*

Committee Member: *Mir Sadri-Sabet*

Committee Member: *Kari Anderson*

Department Chair: *John Gierke*

Table of Contents

Abstract

A relationship between the hydrocarbon migration and magnetic properties of near-surface sediments was investigated from several hundreds of samples collected over the hydrocarbon-bearing Silurian pinnacle reef belt of the Michigan Basin. The collected samples were investigated using several rock magnetic methods and optical microscopy. The investigation has not revealed a straightforward relationship between the magnetic susceptibility and hydrocarbon reservoirs within the reef belt; both anomalously high and low susceptibility values were observed. The elevated values are associated with newly formed magnetite in the form of spheroidal grains produced by hydrocarbon-related diagenesis while the extremely low susceptibilities may reflect dissolution of the originally present hematite. However, a strong correlation was observed between the elevated susceptibility and the gas reservoirs in the Devonian Traverse Group. The obtained results indicate that the magnetic susceptibility method has a hydrocarbon exploration potential but the relevant processes of magnetic mineral diagenesis require additional investigation.

1.0 Introduction

Upward migration of hydrocarbons can cause various chemical and mineralogical changes in the overlying lithologies and sediments, meaning that the rock column above a gas/oil reservoir may acquire significantly different properties from laterally equivalent rocks (Schumacher, 1996; Oehler and Sternberg, 1984; Price, 1986). The hydrocarbon-related alteration of soils and near-surface sediments may produce multiple effects including geochemical and microbiological anomalies, mineralogical transformations, electrochemical changes, magnetic and radiation anomalies, and biogeochemical and geobotanical anomalies (Schumacher, 1996). Based on these effects, various surface exploration methods have been proposed as cost-effective means for selecting targets most favorable for exploration by conventional techniques (Price, 1986). Unfortunately, these methods remain underutilized because the understanding of the complex physical, chemical, and biological processes responsible for hydrocarbon-induced alteration remains incomplete (Machel and Burton, 1991; Abrams, 2005).

The upward migration of hydrocarbons mainly occurs via two mechanisms (Figure 1.1). The first mechanism is effusion (macroseepage) through large subsurface fractures or along fault planes, typically resulting in quasi-linear anomalies with high concentrations of heavy (C_{6+}) hydrocarbons (Price, 1986). The second mechanism is buoyancy-driven microseepage of light (C_{1-6}) hydrocarbon microbubbles (Klusman and Saeed, 1996; Saunders et al., 1999; Brown, 2000), resulting in apical or annular (halo-shaped) anomalies (Madhavi et al., 2011; Schumacher, 2009). Microseepage occurs when the capillary pressure of a gaseous hydrocarbon microbubble exceeds the water displacement pressure

of the cap allowing seal penetration by hydrocarbons (Price, 1986). Although the sediments overlying the reservoir can absorb light hydrocarbons to a certain extent, when this capacity is exceeded, the microbubbles move upward, practically unimpeded. The ascension of microbubbles through microfractures explains near vertical hydrocarbon migration without faulting and macro-fracturing. This can produce geochemical anomalies observed directly over the reservoir such as those reported by Seaman (2002) over the hydrocarbon-bearing pinnacle reefs of the northern Michigan Basin, which also represents a portion of the study area of this project.

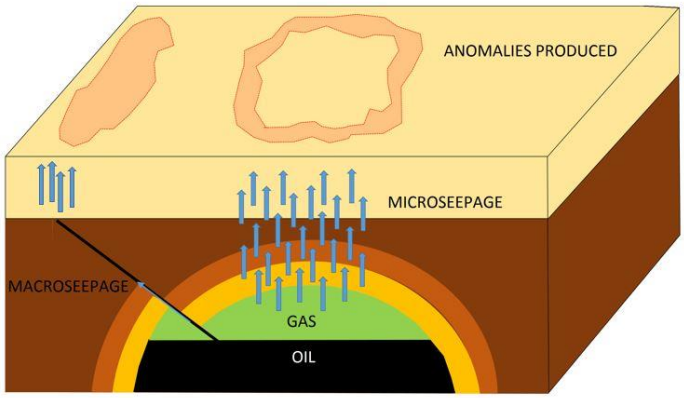

Figure 1.1 A simplified depiction of macroseepage through a fault (left) where hydrocarbon migration path is dependent upon fault orientation versus microseepage (center) where migration is near vertical due to lack of dependence on a conduit as migration path.

This project focuses on the changes in magnetic properties of soils and sediments associated with hydrocarbon seepage. Oil and gas reservoirs are often associated with detectable magnetic anomalies (Foote, 1996; Berger et al., 2002; Liu et al., 2004). The genetic link between these anomalies and hydrocarbon seepage plumes has been supported by general correlation of elevated magnetic susceptibility of soils and sediments with light hydrocarbon gas anomalies (Henry, 1988; Saunders et al., 1991; Ellwood and Burkhart, 1996). There is a general agreement that the magnetic susceptibility enhancement originates from the formation of authigenic magnetic minerals, including magnetite (Fe_3O_4), maghemite (γ-Fe_2O_3), pyrrhotite (Fe_7S_8), and greigite (Fe_3S_4) in the hydrocarbon-

induced reducing environment (Donovan et al., 1979; Elmore et al., 1987; Foote, 1987, 1996; Foote and Long, 1988; Saunders et al., 1991; Reynolds et al., 1990a; Tompkins, 1990; Machel, 2001).

A simplified sequence of the basic processes and reactions resulting in the hydrocarbon-induced magnetic enhancement can be derived from the general models of hydrocarbon-related alteration (Hughes et al., 1986; Price, 1986; Klusman, 1993; Thompson et al., 1994; Machel, 2001). When the upward migrating light hydrocarbons (mainly methane through pentane) reach oxidizing conditions near the surface, they are consumed by hydrocarbon-oxidizing bacteria, hence decreasing oxygen in pore waters:

$$CH_4 + O_2 = CO_2 + H_2O$$

In developed anaerobic conditions, the activity of sulfate reducing bacteria leads to sulfate ion reduction and oxidation of organic carbon to produce reduced sulfur species and bicarbonate ions:

$$2CH_4 + SO_4 = 2HCO_3^- + H_2S$$

$$2CH_2 + SO_4^{2-} = HCO_3^- + HS^- + H_2O + CO_2$$

Highly reactive reduced sulfur species then can combine with available iron to form iron sulfides and oxides. The possible end products of these reactions include pyrite (FeS_2), marcasite (FeS_2), magnetite, pyrrhotite, greigite, or maghemite. For example:

$$Fe_2O_3 + 4H_2S = 2FeS_2 + 3H_2O + 2H^+ + 2e^-$$

$$Fe_2O_3 + 2H_2S = 2FeS_2 + FeO + 2H_2O$$

$$FeO + Fe_2O_3 = Fe_3O_4$$

This generic model, however, does not include all possible processes and reactions which may occur in the chemically and biologically variable near-surface environment (Schumacher, 1996).

The importance of the hematite and iron hydroxides reduction to magnetite mechanism (Donovan et al. 1979) has been supported by occurrences of authigenic magnetite at many hydrocarbon sites (Elmore et al., 1987; McCabe et al., 1987). However, the reduction of sulfates by hydrocarbons either bacterially (bacterial sulfate reduction) or inorganically (thermochemical sulfate reduction) has been shown to be significant in many diagenetic environments (Reynolds et al., 1990a; Machel, 2001), suggesting ferromagnetic sulfides as a possible source of the magnetic anomalies. This mechanism has also been supported by the observation of pyrrhotite and greigite in hydrocarbon seepage environments (Reynolds et al., 1990a; Reyonds et al., 1990b; Goldhaber and Reynolds, 1991; Sassen et al., 1989; Foote, 1996). In addition, the non-magnetic phases, such as pyrite (FeS_2) and siderite ($FeCO_3$) which are commonly found in hydrocarbon-altered environments, can be oxidized to magnetite or maghemite providing another pathway to increased magnetization of rocks (McCabe and Elmore, 1989; Elmore and Crawford, 1990; Ellwood and Burkhart, 1996).

However, the mechanisms of hydrocarbon-related magnetic diagenesis remain poorly understood due to the lack of an extensive and representative observational database. The published studies represent only a small fraction of the possible sedimentary environments and diagenetic pathways (Elmore et al., 1987, Elmore et al., 1993; Sassen et al., 1989; Elmore and Crawford, 1990; Reynolds et al., 1990b; Liu et al., 2004). Additional well-documented case studies are therefore critical to facilitate the fundamental

understanding of the mechanisms of magnetic alteration of the sediments and soils associated with hydrocarbon seepage.

The objective of this project is to produce such an observational dataset by a rigorous investigation of the magnetic properties of sediments and soils overlying the oil-bearing formations of the Silurian northern pinnacle reef belt of the Michigan Basin. The magnetic and iron-contained mineral assemblages are expected to be different in sediments and soils affected and not affected by hydrocarbon alteration. While the former may be represented by strongly magnetic iron oxides (e.g., magnetite) and sulfides (e.g., pyrrhotite), the principal magnetic minerals in intact limestones and shales characteristic for the Michigan Basin are relatively magnetically weak hematite and iron hydroxides (goethite).

2.0 Geological Background

The Michigan Basin is a shallow, intracratonic sag, circular in shape and spanning about 122,000 square miles (316,000 km^2) in the northern central United States and southern Canada (Figures 2.1*a*). The depth to the Precambrian basement in the basin's center is about 14,000 ft (Figure 2.1*b*).

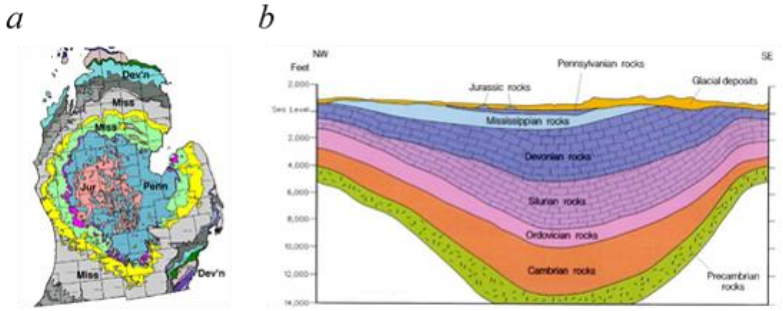

Figure 2.1 *a*) A Simplified bedrock geology map of the Michigan basin. *b*) A generalized section across the Michigan Basin.

The Michigan Basin began subsiding in the Precambrian with the earliest sedimentary strata represented by Cambrian-Ordovician sandstones. However, maximum subsidence occurred during the Late Silurian and Middle Devonian (Cohee and Landes, 1958). During the Middle-Late Silurian (the Niagaran North American stratigraphic stage, ~433-420 Ma), the Michigan Basin was located in the equatorial zone (between the equator and 30°S) (Scotese et al., 1979) and filled with warm water thus creating a shallow sea environment, encouraging reef growth (Briggs, 1974).

During the Niagaran stage, the Michigan Basin consisted of three distinct depositional environments (Figure 2.2): 1) a large central basin of dense micritic, argillaceous limestone, surrounded by 2) a shallow sloping shelf on which small pinnacle reefs developed and interreef micritic crinoidal limestones and nodular limestones were deposited, and further out, 3) a broad basin-edge carbonate bank composed of reef limestone, back-reef lagoonal deposits, patch reefs, and fore-reef lime mudstones and lime sandstones (Mantek, 1973).

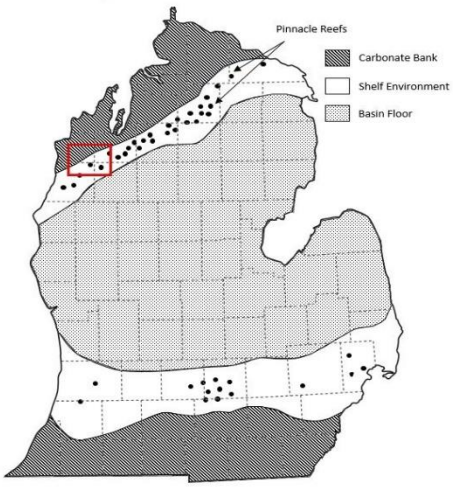

Figure 2.2 Middle and Late Sillurian (Niagaran) depositional environments in the Michigan Basin. The sampling area is indicated by the red box in Northwest corner.

The numerous pinnacle reefs which developed in the transitional region between the outer carbonates and the interior basin contain most of the Silurian oil and gas reserves in the Michigan Basin (Friedman and Kopaska-Merkel, 1991). The primary recoverable reserves in the reefs are estimated at about 350 million barrels of oil and four trillion ft^3 of

natural gas (Gill, 1979). Within the Lower Peninsula of Michigan, the reefs form two bands: a NE trending band in the northern part and an EW in the southern part (Figure 2.2). The target area of this study is within the northwestern arc of the shelf pinnacle reefs (the boxed area in Figure 2.2).

The reefs are relatively small, averaging 0.2 square miles in area, and cover a range of thicknesses from 300 feet to 700 feet. The reefs are laterally contained by evaporites and lime mudstones and overlain by evaporites as well, as shown in Figure 2.3. The depositional history is controversial, but the prevailing model suggests the formation of pinnacles, followed by sea level drop. Subaerial exposure and leaching produced relatively good porosity and permeability, then a hypersaline period produced extensive evaporites that covered and surrounded the pinnacles (Friedman and Kopaska-Merkel, 1991). It is generally agreed that this cycle occurred more than once and that, during some of the evaporite production, porosity generated from leaching was plugged by evaporites, causing inconsistent porosities among pinnacle reefs.

The Silurian carbonates and evaporites are overlain by the Devonian dolostones and limestones with Carboniferous (Mississippian and Pennsylvanian) strata filling the basin center. A relatively thin veneer of Jurassic sediments are locally found in the center of the basin at the surface (Figure 2.1*b*). The area was then covered by glacial till. Within the northern reef band, the Silurian pinnacle reefs are typically found at ~4000-5000 ft. depth, (Figure 2.3).

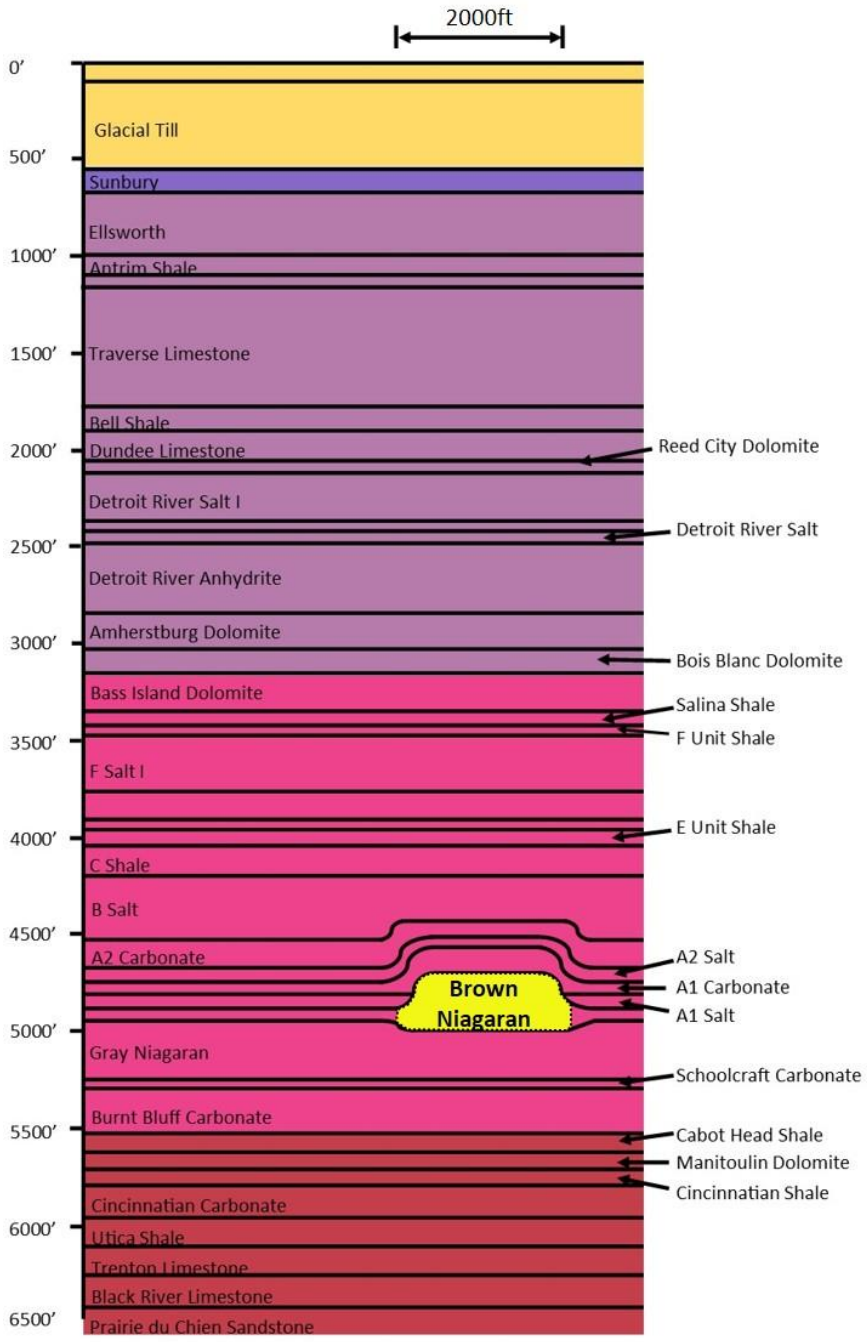

Figure 2.3. Cross sectional view of an average Niagaran pinnacle reef with surrounding formations. Layers are colored by geologic period, with the Ordivician colored subdued red, the Silurian colored dark pink, the Devonian colored grayish purple, then Mississipian Epoch is colored bluish purple, and the Quarternary colored light gold. The Niagaran reef is bright yellow in the center with all dimensions given in feet.

3.0 Methods

3.1 Sampling

Sampling was conducted across the intersection of the northeast corner of Manistee County, the southeast corner of Benzie County, the southwest corner of Grand Traverse County and the northwest corner of Wexford County in the northwestern Lower Peninsula of Michigan. Over the course of four days in August 2016, a total of 264 samples was collected. Sampling sites were generally located at intervals of ~0.6 mi along the county roads to approximate grid coverage. Two samples were taken approximately 15 miles north and one sample was taken approximately 10 miles south from the main area to be used as a regional baseline. Samples were taken between 10-20 meters from the road to avoid road fill or other anthropogenic contamination, and from a depth of approximately

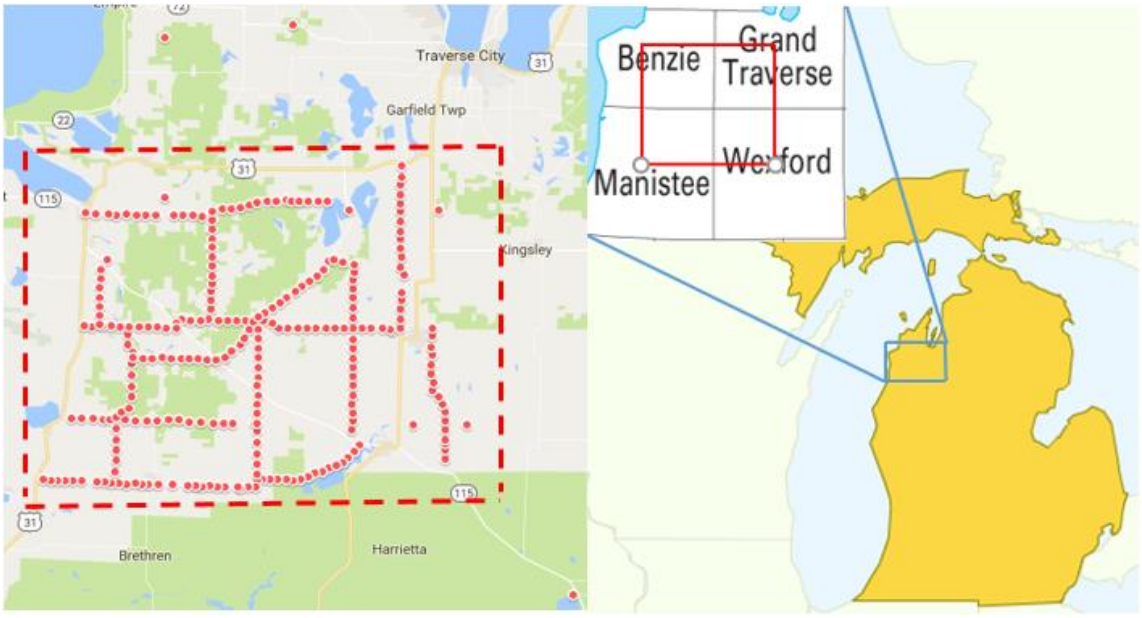

Figure 3.1 Sampling area (right, solid red box) and sampling site locations (left, red circles) in Lower Michigan. Control sites include the two most northerly points and the single point in the southeast corner.

one meter to avoid surface contamination, using an Art's Machine Shop (AMS Inc.) one-piece, four-inch diameter, manual auger. When target depth was reached, the auger was lifted and the sample was taken from the bottom of the auger as quickly as possible to limit exposure to the open air to avoid alteration due to oxidation. Samples were contained in Dynarex sterile, 4oz. specimen cups and stored in a freezer between sampling and measuring phases to reduce alteration.

During sampling, three sediment horizons were observed. Thicknesses varied locally, however the order of occurrence remained constant in the region. The uppermost layer was black, fine-grained material, nearly saturated with water. In very few sampling locations, this layer extended past one half meter depth. The second layer consisted of medium-to-fine-grained white sand with occasional darker inclusions. This layer was also thin, however, it occurred at one meter depth often. The third layer was the most frequent to occur at one meter depth and it was composed of mostly medium-to-fine-grained brown sands with black inclusions.

3.2 Bulk Magnetic Susceptibility

Bulk magnetic susceptibility measurements were conducted using an AGICO (Advanced Geosciences Instruments Company) MFK1-FA magnetic susceptibility meter (kappabridge) equipped with a high-temperature furnace and a cryostat (Figure 3.2). Specimens were prepared by filling plastic (diamagnetic) 8cc cubes with sediment. The masses of the empty cube and the filled cube were both measured to determine the specimens' net mass. Bulk susceptibility was measured by inserting the filled cube into the kappabridge using a special holder (Figure 3.2*a*); the magnetic field applied for

measurement was 200 A/m. Measurements took 1-2 minutes per specimen and were completed in one week. The measured bulk susceptibility values were divided by the net mass of the specimen to find the value of mass-normalized magnetic susceptibility, χ. The obtained data for mass-normalized magnetic susceptibility were used in conjunction with the magnetic susceptibility data measured from a different set of samples from the same sampling area by Kari Anderson in 2013. The values obtained in the previous study were normalized by mass. Both datasets were used to produce a mass-normalized magnetic susceptibility contour map.

After these measurements were completed, the locations and magnetic susceptibility values of the 264 samples from the 2016 sampling excursion were compiled and compared to determine the optimal subset of samples to be used for the rock magnetic investigation. Samples were selected to meet a simple set of criteria. First, samples were chosen to represent the full range of magnetic susceptibility values observed. Second, samples with elevated magnetic susceptibility values were selected such that each region of elevated magnetic susceptibility was represented. Third, several couplings of adjacent samples with a combination of a high and a low magnetic susceptibility value were selected to investigate small scale differences. Lastly, two background samples were selected; one twenty miles north and one twenty miles southeast were chosen to approximate the region not affected by the Silurian pinnacle reefs.

Figure 3.2 Different measurement setups for the MFK1-FA magnetic susceptibility meter (Kappabridge). *a*) Bulk susceptibility measurement of an 8cc cube filled with sediment. *b*) Quartz tube filled with sediment for temperature dependent susceptibility measurement. *c*) Kappabridge equipped with quartz tube containing thermocouple and sample inserted for low-temperature measurement. *d*) Kappabridge equipped with thermostat and quartz tube containing thermocouple and sample inserted for high-temperature measurement.

3.3 Contouring

The contouring process was performed using Surfer 9, and incorporated 420 individual data points with the combined data sets from the 2013 and 2016 sampling excursions. Multiple methods including minimum curvature, inverse distance weighted (IDW) and kriging were attempted and compared to determine the optimal method of contouring that would be utilized. All three methods implemented a regular grid system constructed from known values at sampling locations to interpolate and extrapolate surface information not covered by measured sites. All contouring processes showed similar results, but kriging was ultimately chosen because the semivariogram produced for the isoline computation accounts for accurate estimation over an irregularly spaced grid while also honoring the measured values of χ at sampling locations (Davis, 1986). The IDW and minimum curvature methods approximate the entire surface, causing estimated values to differ from known values at sampling sites for the same locations. The corresponding map produced will be included in the Results section.

3.4 Thermomagnetic Analysis

In order to investigate the magnetic mineralogical composition of the samples, temperature dependencies of low-field magnetic susceptibility, κ-T, were measured upon cycling between room temperature and 700^{o}C, using the AGICO MFK1-FA kappabridge. The κ-T curves were also measured during heating from -192^{o}C to room temperature (a "low-temperature", LT, run) both before and after the high-temperature (HT) thermomagnetic runs (Figure 3.3).

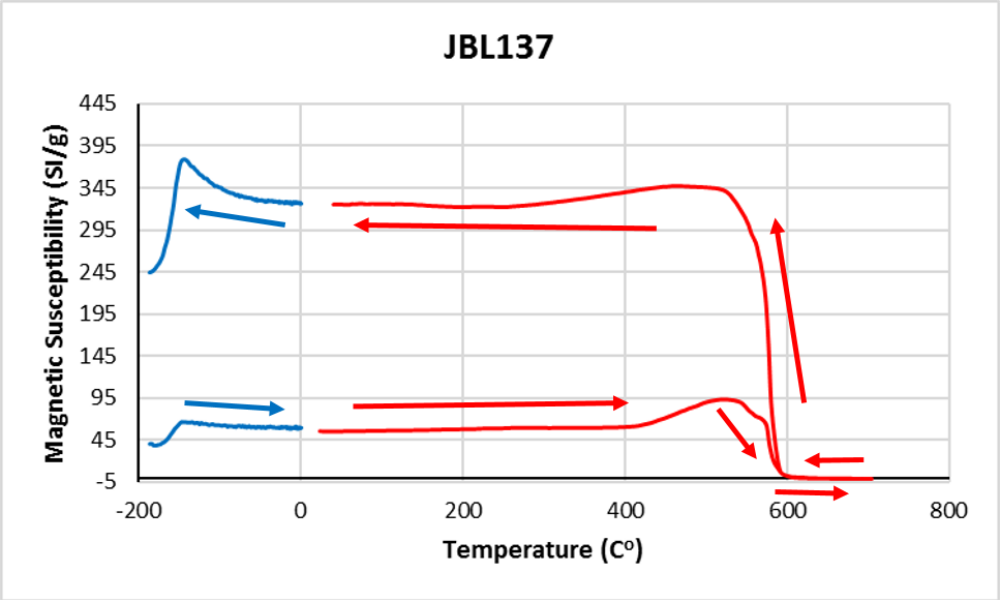

Figure 3.3 Depiction of measurement sequence of temperature dependent magnetic susceptibility. Blue lines indicate low-temperature measurements (L1, L2) and red lines indicate high-temperature measurements (H1). Arrows indicate order of measurements.

For measurement, 350-600 mg of sample material was placed in a specialized quartz tube holder (Figure 3.2*b*) together with a thermocouple to measure the specimen's temperature.

For low temperature measurements of magnetic susceptibility, the quartz holder with sample and thermocouple was inserted into the cryostat and the entire assembly was placed on the arm of the kappabridge (Figure 3.2*c*). The sample was cooled by slowly adding liquid nitrogen to the cryostat until the temperature reached -187.5°C. Then the liquid nitrogen was quickly removed by flushing the system with argon. Measurements were taken at approximately 3°C intervals as the sample was slowly warmed back up to room temperature. The average duration of the low-temperature runs was one hour.

For high-temperature measurements of magnetic susceptibility, the quartz holder with sample and thermocouple was inserted into the furnace and the entire assembly was

again placed on the arm of the kappabridge (Figure 3.2*d*). Magnetic susceptibility was measured upon cycling to 700°C at 7-9°C intervals. The high-temperature runs were conducted with argon flowing through the system to avoid sample oxidation. The average duration of a high-temperature run was about two hours.

After all three runs (LT, HT, LT) were completed, the κ-T data were processed using the Cureval 8.0.2 program provided by AGICO (Chadima and Hrouda, 2012) in order to correct measured susceptibility data by removing the signals from the empty cryostat and the empty furnace. The corrected data were plotted for each sample using Microsoft Excel.

3.5 Magnetic Hysteresis Analysis

The magnetic hysteresis properties were investigated using a MicroMag Model 2900 Alternating Gradient Magnetometer (AGM) which measures the sample's magnetic moment (M) as a function of the applied magnetic field (H), (Figure 3.4*a*). For measurement, a sample (~14-19 mm^3 in volume) is attached to a sample holder and placed between the poles of a water-cooled electromagnet capable of creating magnetic fields within a -1.4 T to +1.4 T range. The AGM uses two additional gradient field coils to create a periodically varying gradient magnetic field in the sample region to induce sample's vibration. The amplitude of this vibration, detected by a symmetrical piezoelectric biomorph, is proportional to the sample's magnetic moment.

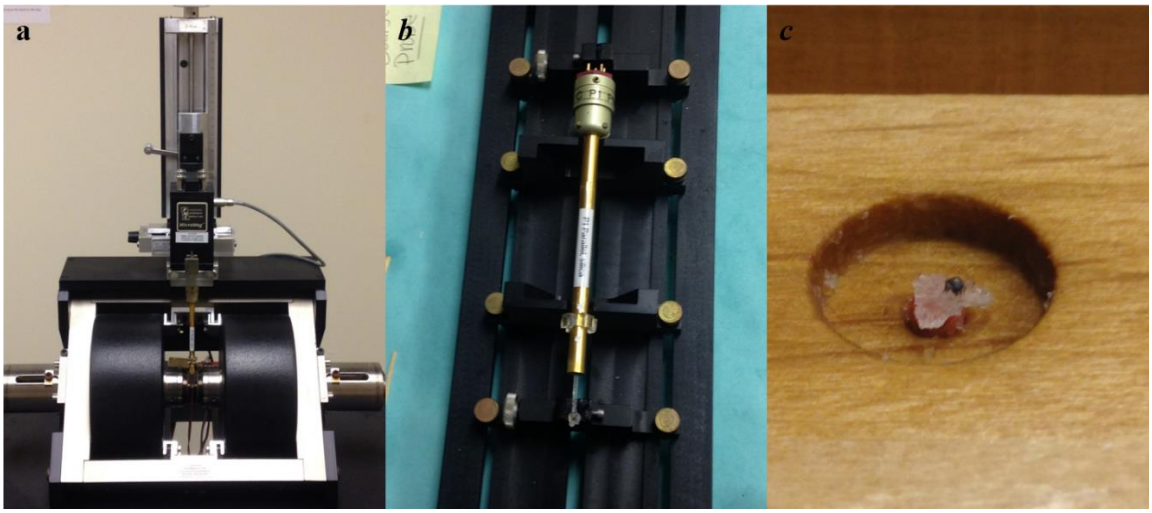

Figure 3.4. Display of probe and setup of AGM for measurement (calibration specifically). *a*) The AGM with probe and calibration standard attached and centered between poles of a water-cooled electromagnet. *b*) Sample probe with the calibration standard adhered to it with silicone grease. *c*) An Yttrium Garnet sphere standard with a magnetic moment of 77.64 μAm^2 used during calibration.

Normally, for AGM measurement, small solid rock chips are attached to the AGM holder stage (3x3 mm^2 in size) using a small amount of diamagnetic silicone grease (Dow Release Compound 7) as adhesive, (Figure 3.4*b*). Between measurements, the stage is wiped with alcohol to remove contamination from the sample and from dust in the air. However, attaching our unconsolidated samples to the stage represented a challenge. Initially, in an attempt to reduce movement of sediment particles relative to each other during measurement, the silicone grease was refrigerated before each measurement to increase its viscosity. Next, approximately 14 mm^3 of sample were mixed with the cold silicone grease and adhered to the probe in the shape of a sphere. However, despite partial success, most curves measured using this approach were still noisy. An alternative solution (shown in Figure 3.5) that yielded the best results consisted in spreading the sample over a

small piece of adhesive tape. A small rectangle containing the sample material was cut, folded over itself and taped again, then attached to the AGM stage using the silicone grease.

Figure 3.5. Display of sample creation using tape to stabilize sediment. *a*) Sediment placed on tape in small amount. *b*) Tape folded over and cut into small rectangle. *c*) Rectangle folded over itself and retaped. *d*) Empty tape rectangle used for empty probe subtraction.

Calibration of the AGM was performed every time after the instrument was turned on (typically once a day) using an yttrium iron garnet sphere standard with a magnetic moment of 77.64 μAm^2 (Figure 3.4*c*). After calibration, a measurement of the empty probe with a small amount of silicone grease adhesive and folded rectangle of tape was performed to determine the background signal ("empty probe") to be subtracted from the data measured from samples.

Magnetic hysteresis measurements (Figure 3.6) consisted of two parts. First, dependence of induced magnetic moment on the applied magnetic field in a magnetic hysteresis loop was measured for the field H ranging from -1.4 T to +1.4 T (the maximum field achievable by the AGM). After a measurement was completed, the raw data were corrected by subtracting the empty probe signal and a further correction was applied to remove the effect of diamagnetic and paramagnetic particles within the sample. AGM

software was then used to calculate the saturation magnetization (M_s), saturation remanent magnetization (M_{rs}), and coercivity (H_c). Second, backfield demagnetization of a saturation remanent magnetization (M_{rs}) was measured. This process involved saturating the sample with a 1.4 T field in one direction, then applying a field in the opposite direction in increments of 50 mT or 100 mT, making a measurement of the remaining remanence (M_r) between each (that is, the measurement is done when the field is off). The entire measurement spanned the range of possible field strength (+1.4T to -1.4T) and the coercivity of remanence (H_{cr}) is obtained by finding the value of magnetic field required to produce an M_r of zero.

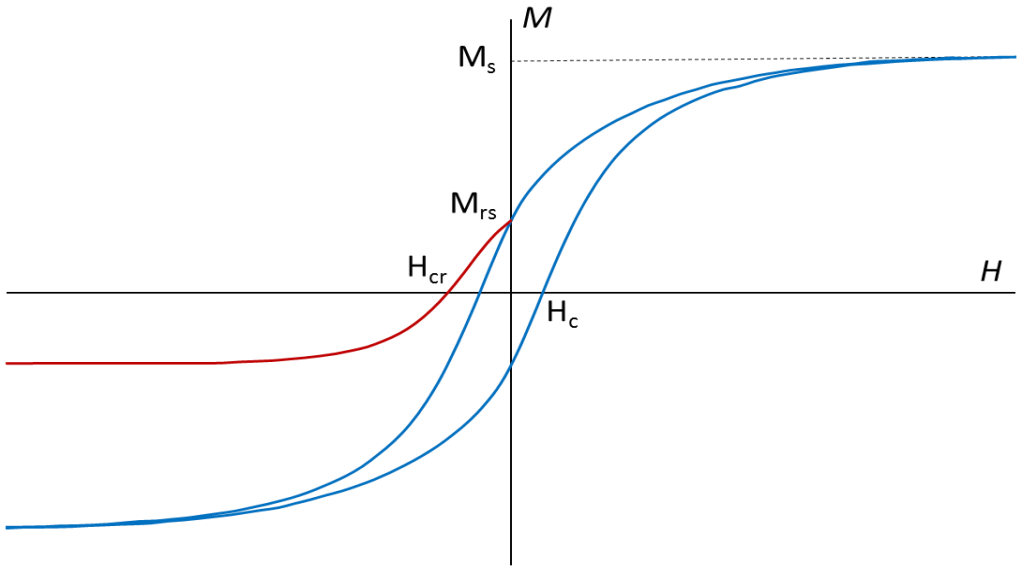

Figure 3.6 Illustration of the magnetic hysteresis parameters determined from a hysteresis loop (blue) and backfield demagnetization measurement (red).

These parameters allow estimation of the domain state of the magnetic minerals present in the samples, which can be used to approximate grain sizes of the magnetic minerals. Domain states are separated into four groups (Figure 3.7). Single domain (SD)

grains are grains small enough to contain one domain, however when the grain size increases, it becomes more energetically favorable to have many domains and this is called multi-domain (MD). When there are few domains, this is called pseudo-single domain (PSD) because, although there are multiple domains, the small number allows the grain to retain some properties similar to SD grains. When the grain size of a SD grain is decreased, there is a point where it loses its ability to retain a magnetic direction without an applied field and these are called superparamagnetic (SP) grains.

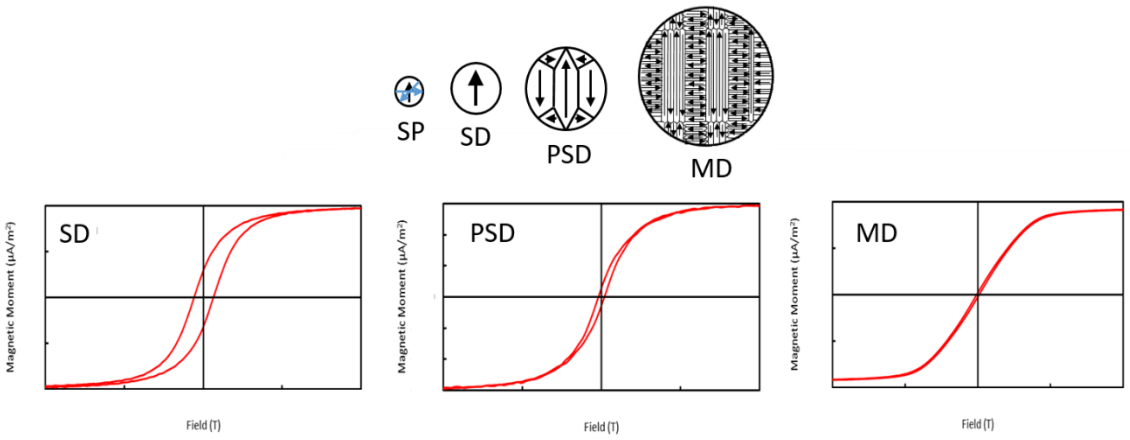

Figure 3.7 Grain size dependence of magnetic domain state and corresponding hysteresis loops.

3.6 Frequency Dependent Magnetic Susceptibility

Superparamagnetic (SP) grains (which are smaller than ~0.03 μm for magnetite) have a magnetic behavior which shows rapid change over time. When SP grains are placed in a magnetic field, and then removed, they lose the induced magnetization received in a very short period of time; about 1/10000th of a second. This is because the natural thermal

energy in ultrafine SP grains is sufficiently strong to overcome the energy induced by a magnetic field (Dunlop and Özdemir, 1997).

The measurement of frequency dependent susceptibility exploits this phenomenon by measuring a sample at two or more magnetization frequencies. A low frequency (976 Hz) measurement (the standard susceptibility measurement χ_{lf}) allows the SP grains close to the boundary with stable SD (SSD) grains to contribute fully to susceptibility, whilst a higher frequency measurement (3904 Hz or 15616 Hz) does not. The higher frequency has the effect of shifting the domain boundary between SP and SSD grains to smaller crystal sizes. Thus SP grains close to the boundary behave like SSD grains with a lower susceptibility value. The difference in the values of the two measurements at different frequencies indicates the presence and relative amount of superparamagnetic minerals (Maher, 1988).

Frequency dependence of magnetic susceptibility was measured using the AGICO MFK1-FA kappabridge utilizing the same procedure and setup as the bulk susceptibility measurements, implementing all three frequencies possible by the instrument: 976 Hz, 3904 Hz, and 15616 Hz. Measurements were completed in 1-2 minutes per sample. Once all measurements at one frequency were completed, the instrument frequency was increased and a ten minute period was needed for stabilization. Upon completing measurements, percentage frequency dependent susceptibility (k_{fd}%) was estimated using the following formula:

$$\kappa_{fd}\% = (\kappa_{lf} - \kappa_{hf}/\kappa_{lf}) \times 100 \qquad (3.1)$$

where κ_{lf} is the magnetic susceptibility measured at low frequency (976 Hz) and κ_{hf} is the magnetic susceptibility measured at high frequency (15616 Hz).

3.7 Optical and Scanning Electron Microscopy

Visual inspection of the samples was performed using a [insert microscope name], implementing magnifications of two, four, ten and 20 times (2x, 4x, 10x, 20x, respectively). Small portions of each sample (~10mm^3) were spread across a clear petri dish and viewed under 2x magnification to identify any simple correlations between samples. While viewing the samples in this way, a magnet was also used to identify magnetic mineral grains within the samples. Upon identification, magnetic minerals were investigated further with higher magnifications.

Several samples expressing a range of magnetic susceptibility values were also selected for viewing in a JEOL 6400 Scanning Electron Microscope (SEM) located in the Michigan Technological University Applied Chemical and Morphological Analysis Laboratory (ACMAL). Of these samples, three also underwent a magnetic extraction process to limit the grains viewed with the SEM to those that are magnetic. This process involved mixing a finely ground sample with distilled water in a small vial. After mixing, glass tube containing a magnet was inserted to attract the mineral grains of interest. After removed from the vial, the magnet was taken out of the glass tube and distilled water was used to wash the magnetic grains onto a clean petri dish. The samples were then placed in a clean environment while the water evaporated. This process was conducted several times on each sample. [IMAGE]

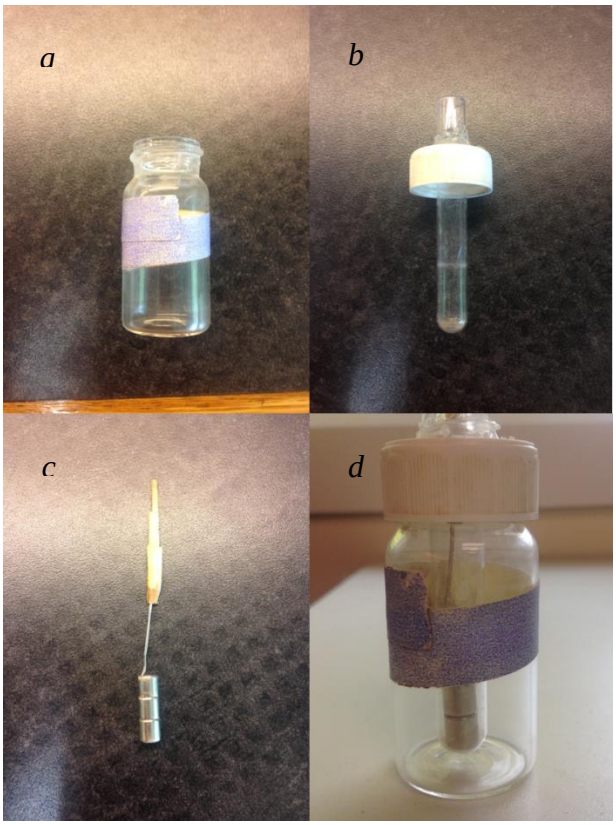

Figure 3.8 Magnetic extraction tool components and assembly. The tool is comprised of a *a*) small vial, *b*) a cap with a tube attached, and *c*) a magnet attached to a shaft. *d*) Assembled tool.

4.0 Results

4.1. Mass-Normalized Bulk Magnetic Susceptibility

The mass-normalized magnetic susceptibility (χ) data from the samples collected in both 2013 and 2016 showed a right-skewed distribution (Figure 4.1). The bulk susceptibilities ranged from 0.282 μSI/g to 145 μSI/g with a mean of 26.8 μSI/g and a median of 20.6 μSI/g. The values from three samples collected to obtain a regional background ("controls") were within 10.7-20.5 μSI/g with an average value of 16.3 μSI/g. The complete table of mass-normalized magnetic susceptibility values is provided in Appendix A.

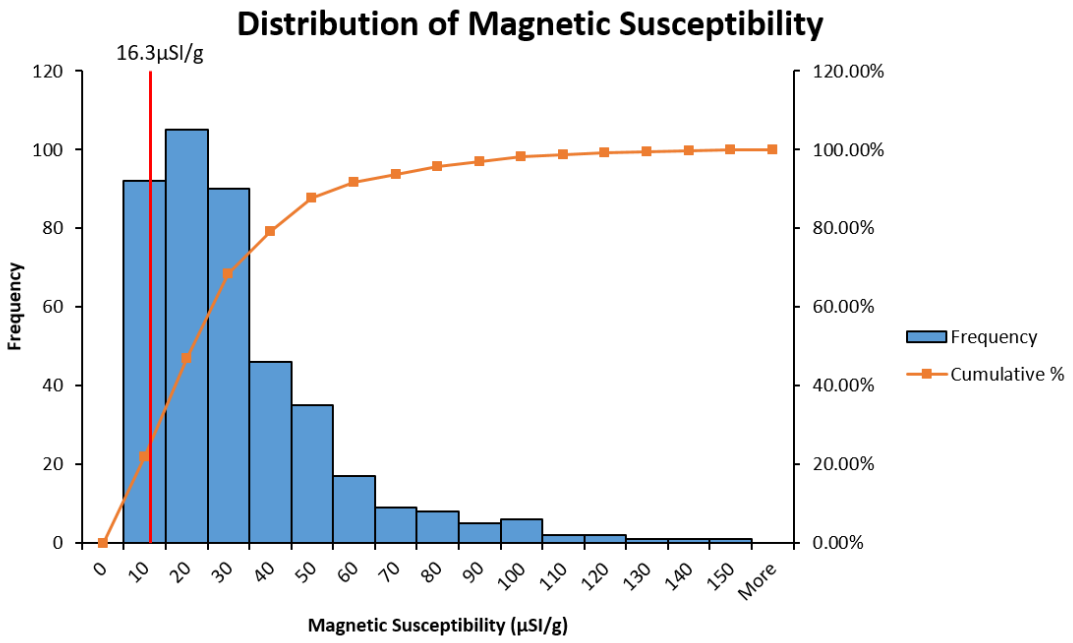

Figure 4.1 Histogram and cumulative distributions function (orange line) of mass-normalized magnetic susceptibility values measured from the samples collected in 2013 and 2016. The red line indicates the average mass-normalized susceptibility of the background samples.

4.2 Contouring

The combined dataset of mass-normalized susceptibility values was used to create a contour map of χ over the sampled region (Figure 4.2*a*). The map shows two relatively large regions of elevated (>75 μSI/g) magnetic susceptibility. One region extends from the center into the northeastern quadrant. The significance of this region is corroborated by its correlation with the high susceptibility values measured from the individual samples collected within that area (Figure 4.2*b*).

The other region is located in the northwestern corner of the map. However, the significance of the second region is questionable because no samples were collected within that area (northwest of 4941000 m north, 572000 m east). Instead, the elevated

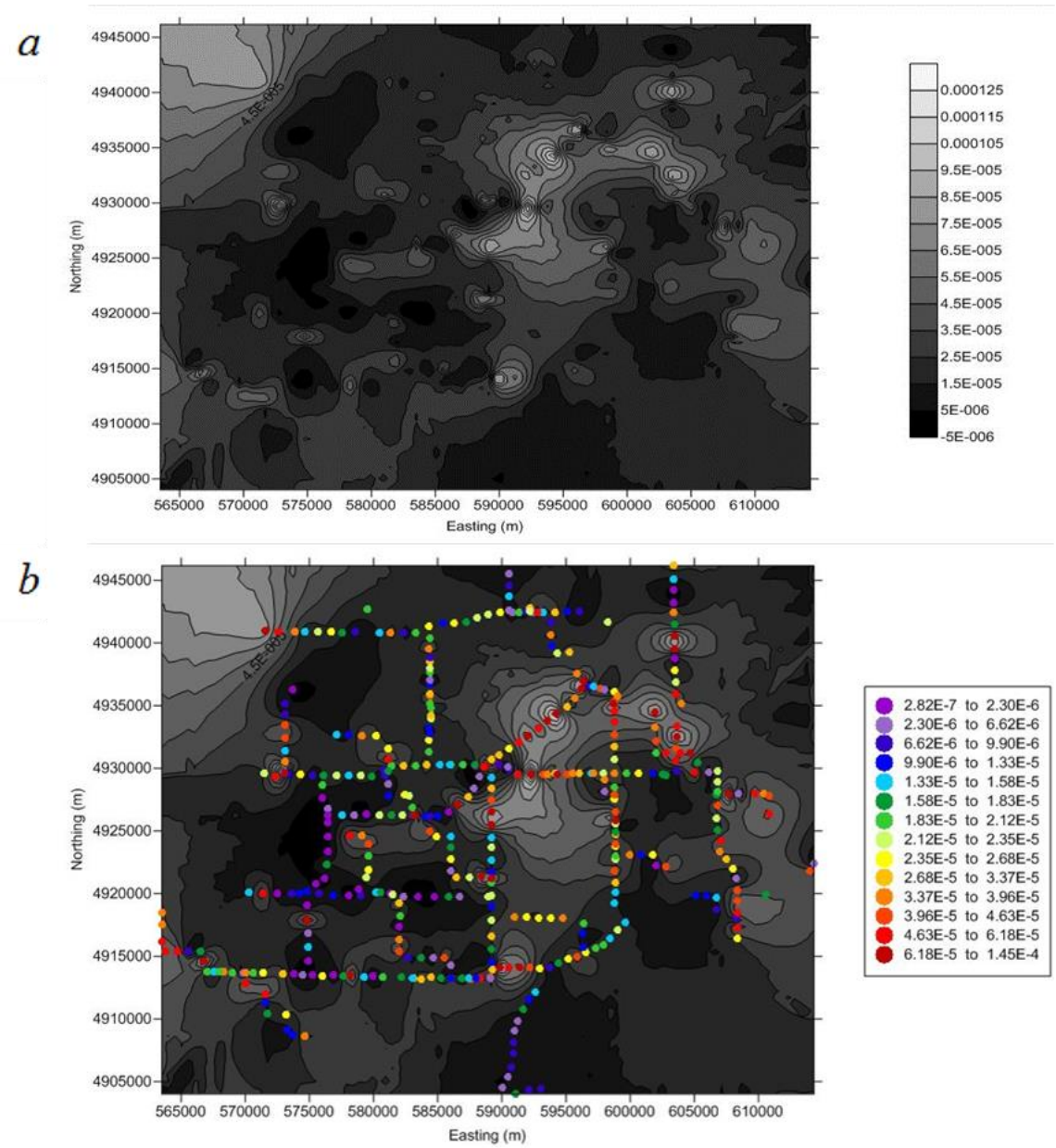

Figure 4.2 *a*) A contour map of mass-normalized magnetic susceptibility (χ) over the surveyed area: darker areas indicate lower values and lighter area indicate higher values of χ. ***b*)** The same contour map overlain with the sampling site locations (for both 2013 and 2016 sampling excursions). The point color corresponds to the susceptibility value measured from the respective individual site: cold colors indicate low values and hot colors indicate high values. The scale bar units are SI/g.

susceptibility contours in the NW corner are generated by the contouring algorithm based on the increasingly high values measured from the closest sampling sites (Figure 4.2*b*).

In addition, the map reveals several much smaller areas of elevated χ (for example, the area centered at approximately 4930000N, 572500E, in the NW quadrant).

4.3 Thermomagnetic Analysis

The temperature dependencies of low-field magnetic susceptibility ($\kappa(T)$) were measured from nineteen sites representing the full range of measured bulk magnetic susceptibilities. These measurements allow the identification of magnetic minerals present in the samples by identifying both the Curie temperature of the material (the temperature where ferromagnetism is lost), as well as some unique low-temperature magnetic mineral phase transitions. All measured samples yielded irreversible $\kappa(T)$ curves characterized by a substantial increase in susceptibility upon heating (Figures 4.3-4.6). The samples with very low initial bulk susceptibilities (e.g., JBL37, JBL77, JBL199) yielded noisy low-temperature $\kappa(T)$ curves but, in most cases, the curves were interpretable. In addition, two samples with the lowest initial bulk susceptibility (JBL37 and JBL77) manifested a decrease in susceptibility near 480°C causing negative $\kappa(T)$ values (Figure 4.3) . However, upon closer inspection, it was determined that this minimum is likely to be an artefact caused by subtracting the signal of the empty furnace, which is comparable with the sample susceptibility.

For all but three samples (JBL71, JBL77, and JBL260), the first low-temperature run showed a peak at ~-150°C which corresponds to the Verwey transition in magnetite (T_V = -151°C), indicating the presence of nearly-stoichiometric magnetite (Verwey, 1939). For

all but one (JBL37) sample, the high-temperature κ(T) curves show an increase at about 450°C, followed by a large decrease near 585°C, the Curie temperature of magnetite, thus indicating the presence/formation of magnetite upon heating. The broad peaks between ~450°C and 580°C vary in magnitude, with increases in magnetic susceptibility ranging from ~20% up to ~500% (JBL127) within a ~100°C interval. Many of the samples manifested more pronounced Verwey transition peaks during the second low-temperature run, indicating the formation of new magnetite during heating. New formation of magnetite is likely to be caused by oxidation of pyrite (Krs et al., 1992).

Several samples, most noticeably JBL150 and JBL204, also display a smaller bump around 250-320°C, which could indicate either the presence of pyrrhotite (Tc ~ 320 °C) or the formation of maghemite and its destruction at 300-350 °C (a slight decrease of κ). Both samples selected from outside of the area expected to be affected by the pinnacle reef belt hydrocarbon reservoirs (JBL260 and JBL264) also displayed weak Verwey transitions in the initial low-temperature runs, as well as an increase in Verwey transition expression between the first and second low-temperature runs. This indicates that the regional background may contain detrital magnetite, however the expression of the Verwey transition in the initial low-temperature run was difficult to distinguish (especially in JBL260, Figure 4.6), and so detrital magnetite is likely in small amounts.

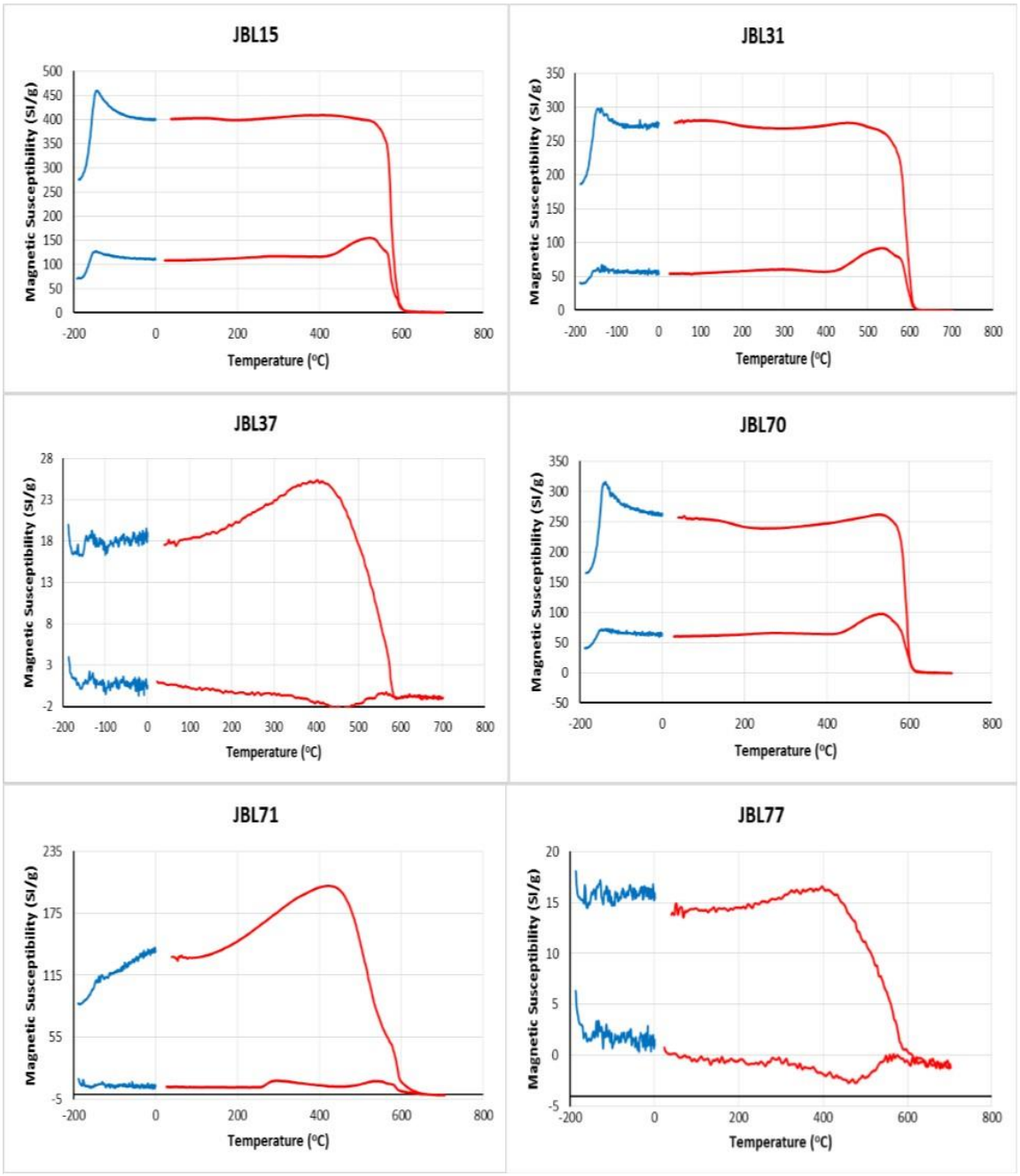

Figure 4.3 Temperature dependent magnetic susceptibility measurements for samples JBL15, JBL31, JBL37, JBL70, JBL71 and JBL77. Low-temperature runs are shown in blue and high-temperature runs are shown in red for each sample.

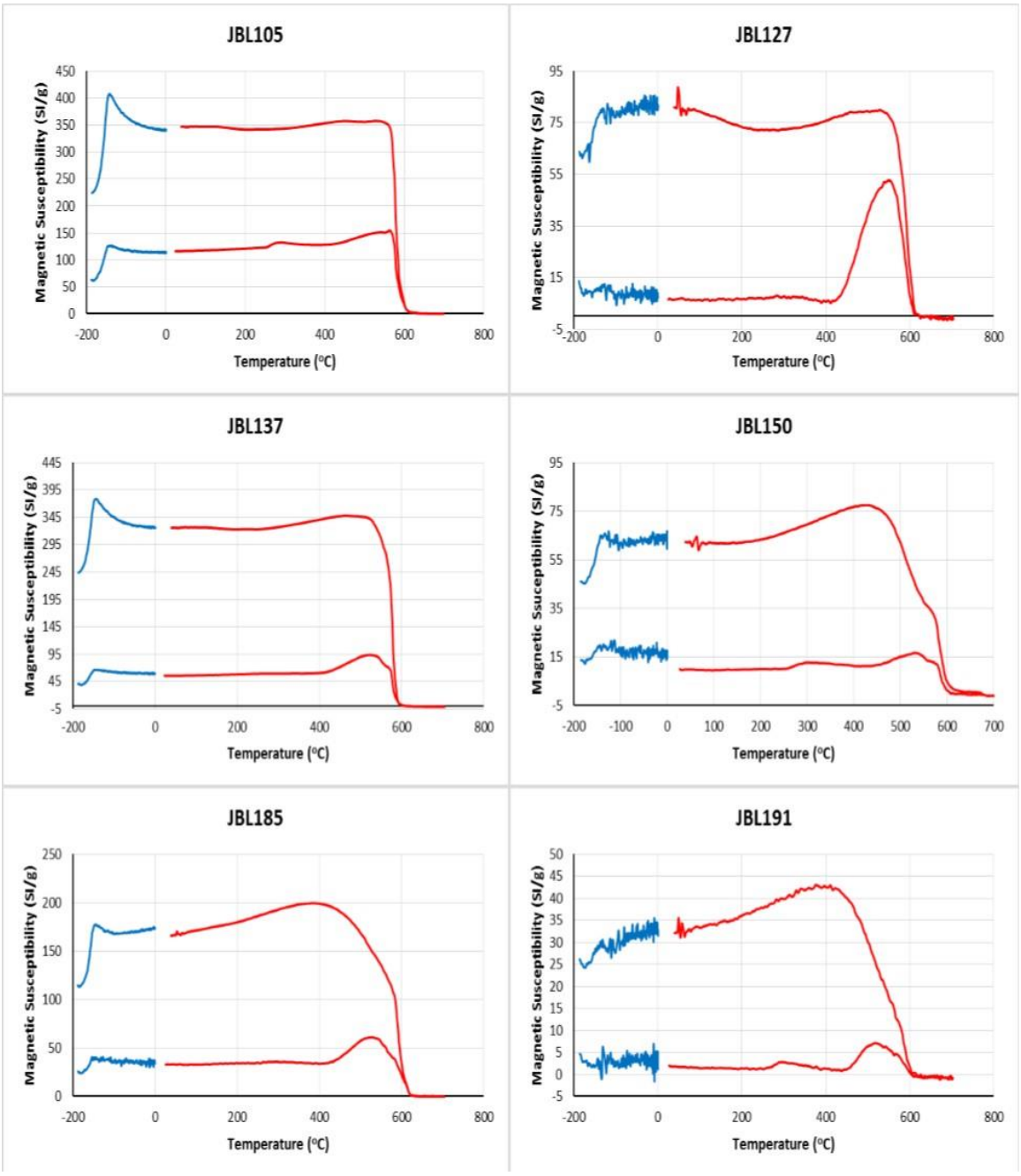

Figure 4.4 Temperature dependent magnetic susceptibility measurements for samples JBL105, JBL127, JBL137, JBL150, JBL185 and JBL191. Low-temperature runs are shown in blue and high-temperature runs are shown in red for each sample.

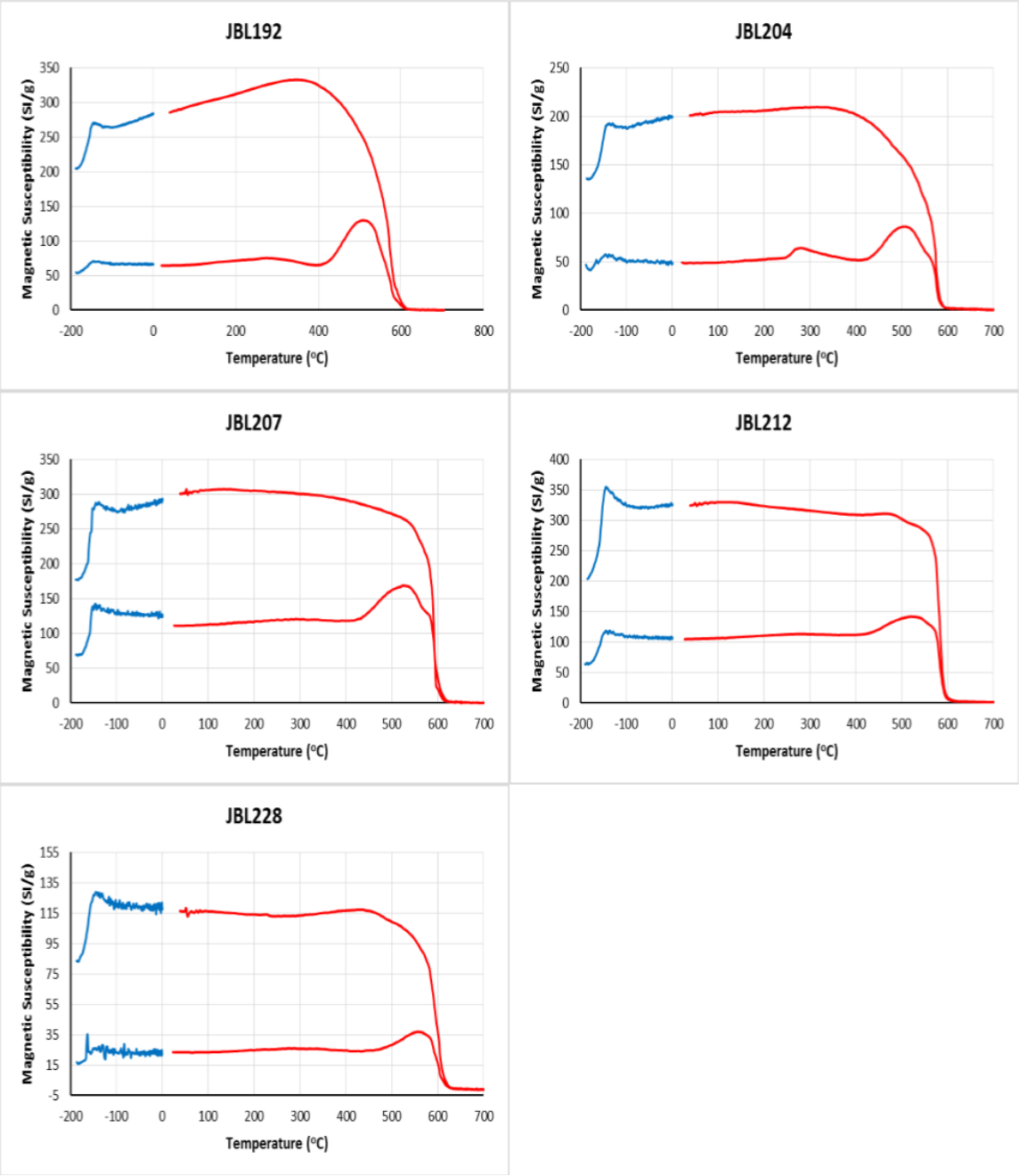

Figure 4.5 Temperature dependent magnetic susceptibility measurements for samples JBL192, JBL204, JBL207, JBL212, and JBL228. Low-temperature runs are shown in blue and high-temperature runs are shown in red for each sample.

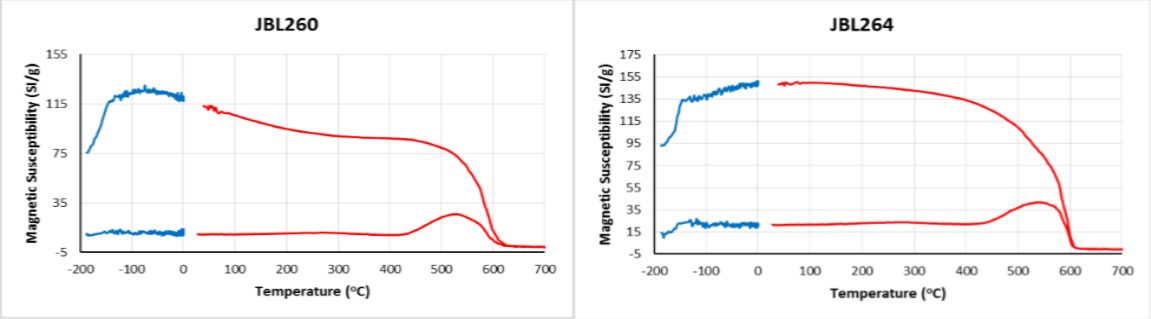

Figure 4.6 Temperature dependent magnetic susceptibility measurement for background samples JBL260 and JBL264. Low-temperature runs are shown in blue, while the high-temperature run is shown in red.

4.4 Magnetic Hysteresis Analysis

The magnetic hysteresis data were measured from 49 specimens representing 19 different samples (Table 4.1) and all measured curves can be found in the Appendices. The samples for hysteresis analyses were selected to represent the full range of the mass-normalized magnetic susceptibilities (~0-145 μSI/g) observed over the entire study area (Table 4.1; Figure 4.2). Many samples manifested heterogeneity of the magnetic hysteresis properties measured from different specimens (e.g., sample JBL15, Table 4.1, Figure 4.7) which most likely reflects the heterogeneity of sample material. Several specimens displayed varying degrees of "wasp-waisted" behavior (Roberts et al., 2000), where the curves are constricted in the middle section and wider above and below (Figure 4.8). Such a behavior suggests the presence of mixtures of magnetically hard and soft magnetic particles, or a mixture of superparamagnetic and single-domain particles. Several other samples failed to saturate in a 1.4 T magnetic field, indicating the presence of a magnetically hard mineral such as hematite or goethite.

All the measured specimens exhibited pseudo-single-domain (PSD) to multi-domain (MD) behavior dominated by relatively low M_{rs}/M_s (squareness) ratios ranging from 0.005 to 0.184, and high H_{cr}/H_c ratios ranging from 2.13 to 176 (Table 4.1; Figure 4.9*a*). However, the magnetic moments of 16 (of 49) measured specimens were relatively weak resulting in noisy hysteresis curves which could affect the estimated values of magnetic hysteresis parameters. This problem was especially noticeable for the backfield remanence measurements so that the coercivity of remanence (H_{cr}) and, hence, the H_{cr}/H_c values obtained for these samples could be biased.

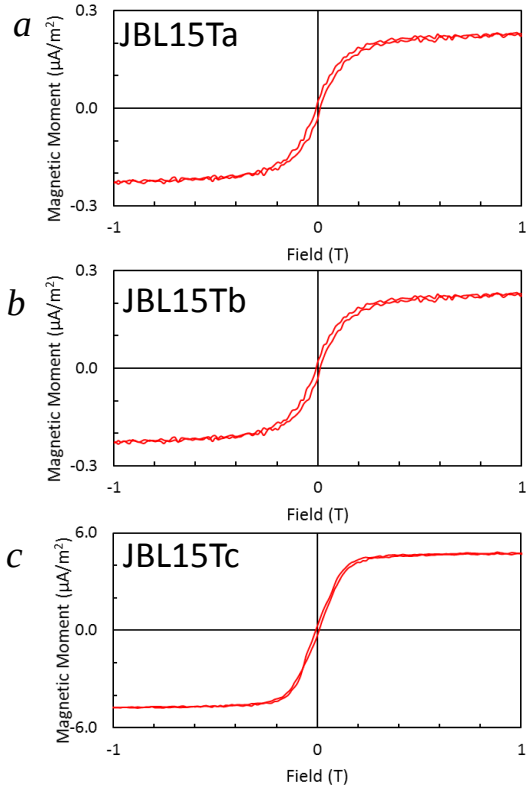

Figure 4.7 Magnetic hysteresis loops measured from three different specimens of Sample JBL15 displaying material heterogeneity within the sample. The values of M_s and M_{rs} /M_s ratios are noticeably different between *a*) 226.3 nAm2 and 0.112, *b*) 914.8 nAm2 and 0.084, and *c*) 4752 nAm2 and 0.063, respectively (Table 4.1). Note that the horizontal axes are truncated at ±1 T.

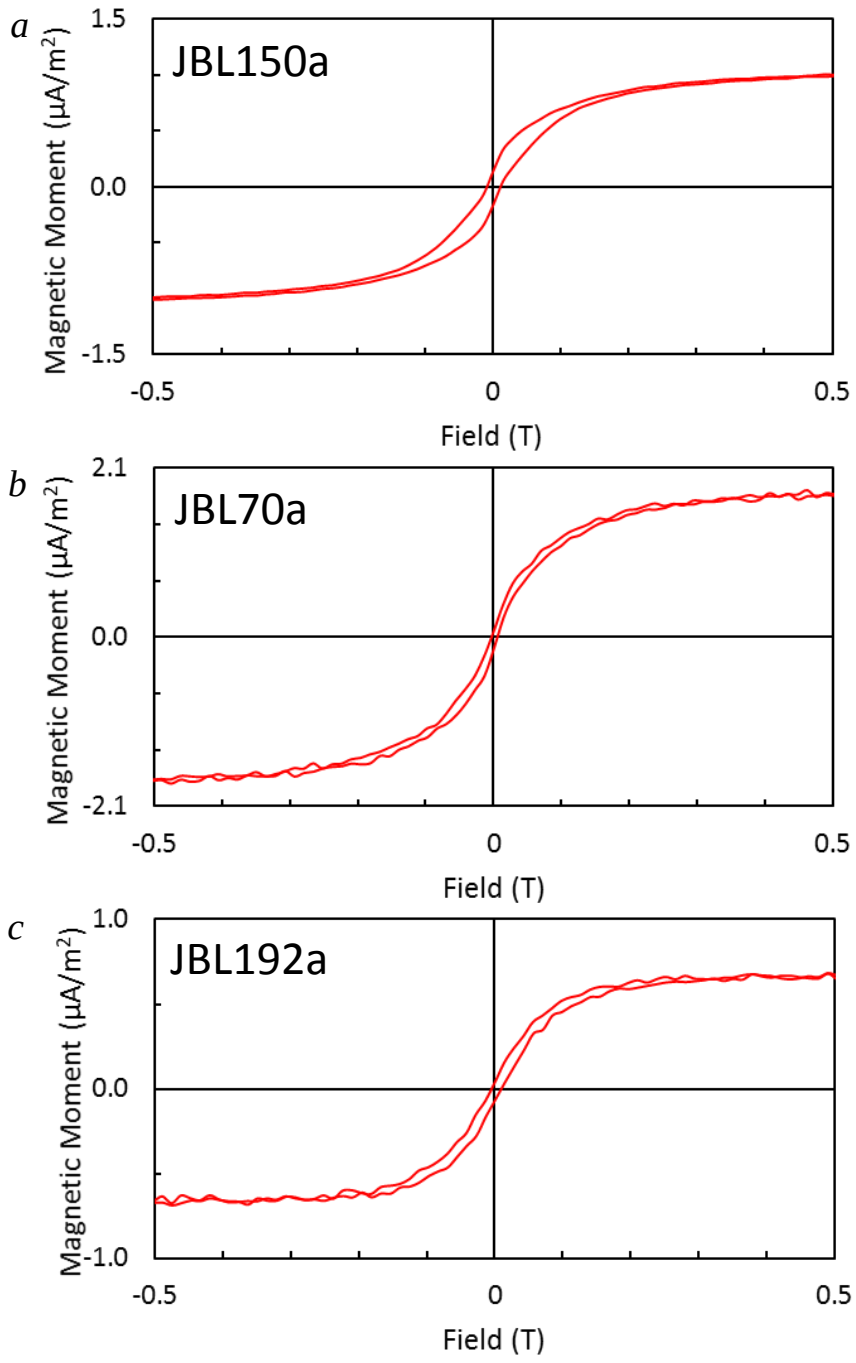

Figure 4.8 Magnetic hysteresis loops displaying various degree of the "wasp-waisted" behavior. *a*) Sample JBL150Tb shows very pronounced "wasp-waisted" behavior. *b*) Sample JBL70a appears nearly closed at the origin with a slightly greater separation at the top and bottom of the curve. *c*) Sample JBL192a displays further broadening than JBL70a, though still closer to the top and bottom of the curve. Note that the horizontal axes are truncated at ±0.5 T to emphasize the behavior in the central region.

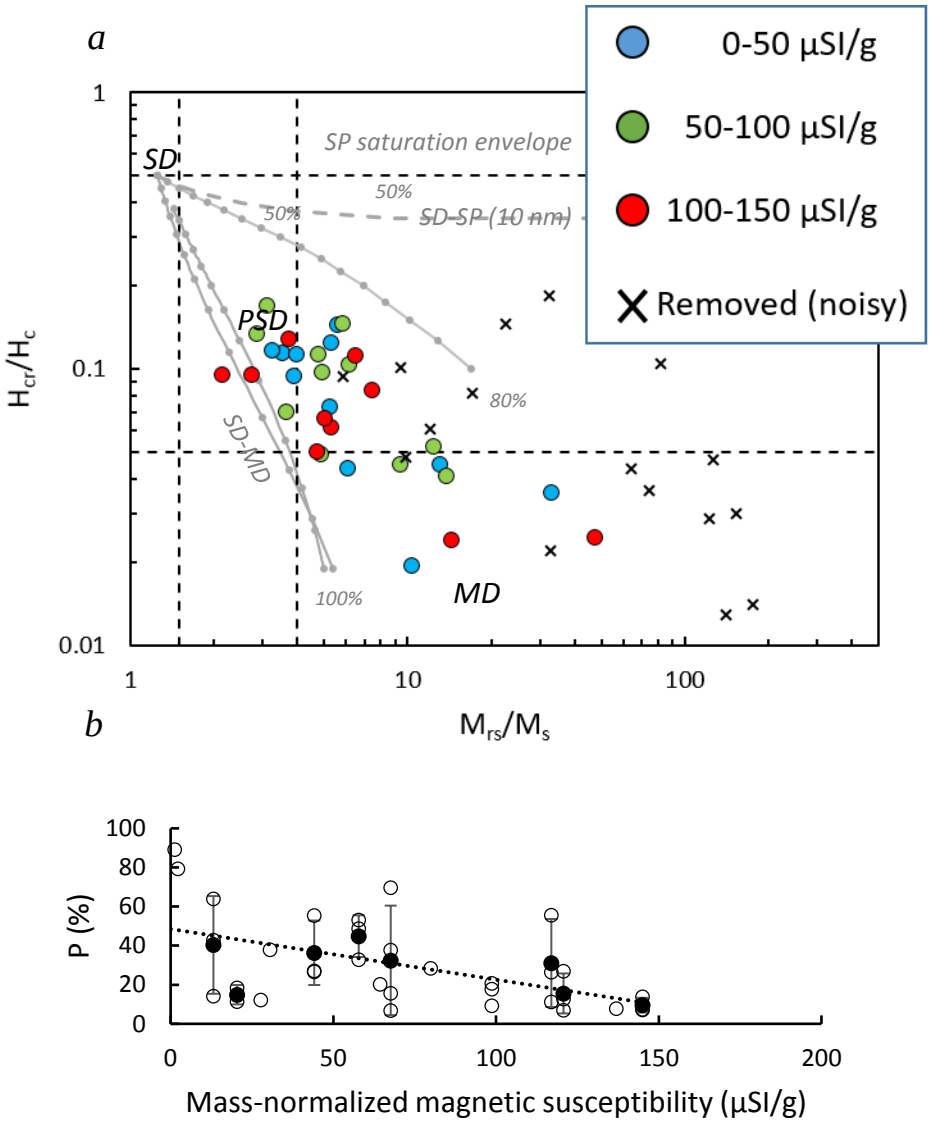

Figure 4.9 *a*) Magnetic hysteresis ratios plotted on Day diagram (Day et al., 1977). Gray lines are theoretical curves for mixtures of MD and SD grains (MD-SD lines, based on two different models), and SP (10 nm in size) and SD grains (SD-SP line) after Dunlop (2002). Numbers along curves are volume fractions of SP or MD component in mixtures with SD grains. Dashed gray line shows SP saturation envelope. *b*) Dependence of the relative paramagnetic contribution, P (see text), on the mass-normalized magnetic susceptibility. Open circles show individual sample data and closed circles show sample-mean values (Table 4.1). The error bars are 1 σ. Dotted line is the best-fit line based on the individual data points.

Table 4.1 Magnetic hysteresis data: H_c: Coervice force; M_{rs}: saturation remanence; M_s: saturation magnetization; H_{cr}: coervicity of remanence; P: relative paramagnetic fraction of the total saturation magnetization M_{s_total} [P(%) = (1 – M_s/M_{s_total}) x 100%]; χ: mass-normalized magnetic susceptibility. Asterisks indicate the low signal-to-noise ratio data excluded from the interpretation and Figures 4.9*a*, 4.10, and 4.11. Uncertainties shown are 1σ.

Sample	**H_c (mT)**	**M_{rs} (nAm^2)**	**M_s (nAm^2)**	**H_{cr} (mT)**	**M_{rs}/M_s**	**H_{cr}/H_c**	**P (%)**
χ = 117.0 μSI/g							
JBL15Ta	9.8	25.4	226.3	63.4	0.112	6.5	55.6
JBL15Tb	8.1	76.7	914.8	59.7	0.084	7.4	26.5
JBL15Tc	7.9	294.4	4752.0	41.9	0.062	5.3	11.3
Mean	**8.6 ± 1.0**	**132.2 ± 142.8**	**1964.4 ± 2438.6**	**55 ± 11.5**	**0.086 ± 0.025**	**6.4 ± 1.1**	**31.1 ± 22.5**
χ = 67.6 μSI/g							
JBL31Ta	15.4	109.9	818.2	44.1	0.134	2.9	15.6
JBL31Tb	12.1	70.9	679.2	73.8	0.104	6.1	37.7
JBL31Tc	6.4	193.9	3951.0	30.9	0.049	4.8	6.8
JBL31Td	11.7	7.2	102.8	42.6	0.070	3.6	69.7
Mean	**11.4 ± 3.7**	**95.5 ± 78.1**	**1387.8 ± 1736.6**	**47.8 ± 18.3**	**0.090 ± 0.038**	**4.4 ± 1.4**	**32.4 ± 28**
χ = 1.1 μSI/g							
*JBL37Tb**	*13.6*	*6.6*	*35.9*	*439.8*	*0.184*	*32.3*	*87.7*
χ = 64.6 μSI/g							
*JBL70Ta**	*15.7*	*90.3*	*618.7*	*356.2*	*0.146*	*22.7*	*26.9*
*JBL70Tb**	*4.4*	*111.6*	*1830.0*	*53.3*	*0.061*	*12.0*	*7.3*
JBL70Tc	6.7	26.0	633.9	91.7	0.041	13.8	20.3
χ = 1.3 μSI/g							
*JBL71Ta**	*14.2*	*4.7*	*46.6*	*134.5*	*0.101*	*9.4*	*81.9*
JBL71Tb	0.2	0.2	44.1	35.2	0.005	149.1	89.2
χ = 0.9 μSI/g							
*JBL77Ta**	*5.1*	*1.0*	*20.8*	*649.6*	*0.047*	*126.6*	*90.5*
*JBL77Tb**	*10.1*	*3.3*	*75.1*	*652.7*	*0.043*	*64.4*	*60.4*
χ = 145.0 μSI/g							
JBL105Ta	3.1	27.3	1104.0	144.9	0.025	47.4	7.5
JBL105Tb	5.0	179.6	3575.0	23.6	0.050	4.7	13.9
JBL105Tc	9.5	428.1	4476.0	20.1	0.096	2.1	7.2
Mean	**5.9 ± 3.3**	**211.7 ± 202.3**	**3051.7 ± 1745.9**	**62.9 ± 71.1**	**0.057 ± 0.036**	**18.1 ± 25.4**	**9.5 ± 3.8**

Table 4.1 (Cont'd)

Sample	H_c (mT)	M_{rs} (nAm^2)	M_s (nAm^2)	H_{cr} (mT)	M_{rs}/M_s	H_{cr}/H_c	P (%)
χ = 13.1 μSI/g							
JBL127Ta	1.2	11.6	324.3	39.6	0.036	32.8	14.2
*JBL127Tb**	*10.9*	*8.5*	*89.7*	*63.6*	*0.094*	*5.8*	*38.1*
JBL127Tc	8.7	15.6	213.0	45.3	0.073	5.2	42.9
JBL127Td	12.4	6.1	53.5	43.6	0.115	3.5	64.0
Mean (n=3)	**7.4 ± 5.7**	**10.5 ± 4.1**	**170.1 ± 123.4**	**48 ± 10.7**	**0.080 ± 0.034**	**11.8 ± 14**	**39.8 ± 20.4**
χ = 137.0 μSI/g							
*JBL137Ta**	*8.8*	*59.3*	*1235.0*	*86.3*	*0.048*	*9.8*	*16.3*
JBL137Tb	9.9	119.4	1793.0	49.3	0.067	5.0	7.9
χ = 30.6 μSI/g							
*JBL150Ta**	*5.2*	*68.9*	*3134.0*	*169.8*	*0.022*	*32.8*	*6.9*
JBL150Tb	10.3	150.0	1040.0	57.4	0.144	5.6	38.0
χ = 98.7 μSI/g							
*JBL185Ta**	*4.7*	*108.2*	*2960.0*	*349.2*	*0.037*	*74.0*	*9.2*
*JBL185Tb**	*1.8*	*18.2*	*1406.0*	*260.1*	*0.013*	*140.8*	*17.8*
JBL185Tc	18.2	263.4	1542.0	56.1	0.171	3.1	20.8
χ = 2.2 μSI/g							
JBL191Ta	9.9	5.6	59.1	38.5	0.094	3.9	79.4
*JBL191Tb**	*2.0*	*21.4*	*1528.0*	*353.4*	*0.014*	*175.8*	*4.3*
χ = 79.9 μSI/g							
*JBL192Ta**	*7.3*	*54.0*	*657.6*	*124.4*	*0.082*	*17.1*	*49.5*
JBL192Tb	5.8	72.9	1385.0	71.8	0.053	12.4	28.5
JBL192Tc	12.2	54.6	373.3	70.3	0.146	5.8	
Mean (n=2)	**9.0 ± 4.5**	**60.5 ± 10.7**	**805.3 ± 521.8**	**88.8 ± 30.8**	**0.094 ± 0.048**	**11.8 ± 5.7**	**39 ± 14.8**
χ = 57.8 μSI/g							
JBL204Ta	5.5	48.2	1066.0	51.8	0.045	9.4	32.8
JBL204Tb	13.8	37.6	385.5	67.8	0.097	4.9	53.1
JBL204Tc	11.7	54.8	486.5	55.8	0.113	4.8	48.7
Mean	**10.3 ± 4.3**	**46.9 ± 8.7**	**646 ± 367.2**	**58.4 ± 8.3**	**0.085 ± 0.035**	**6.4 ± 2.6**	**44.9 ± 10.7**
χ = 44.2 μSI/g							
JBL207Ta	12.4	66.4	586.4	49.3	0.113	4.0	27.1
JBL207Tb	5.4	29.3	646.9	70.9	0.045	13.0	26.6
JBL207Tc	11.0	26.7	227.5	35.4	0.118	3.2	55.4
Mean	**9.6 ± 3.7**	**40.8 ± 22.2**	**486.9 ± 226.7**	**51.9 ± 17.9**	**0.092 ± 0.041**	**6.7 ± 5.5**	**36.4 ± 16.5**

Table 4.1 (Cont'd)

Sample	H_c (mT)	M_{rs} (nAm^2)	M_s (nAm^2)	H_{cr} (mT)	M_{rs}/M_s	H_{cr}/H_c	P (%)
χ = 120.7 µSI/g							
JBL212Ta	4.1	133.4	5553.0	59.0	0.024	14.3	7.0
JBL212Tb	11.1	89.8	698.5	41.1	0.129	3.7	26.9
JBL212Tc	6.8	180.3	1890.0	18.5	0.095	2.7	12.7
Mean	**7.3 ± 3.5**	**134.5 ± 45.3**	**2713.8 ± 2529.9**	**39.5 ± 20.3**	**0.083 ± 0.053**	**6.9 ± 6.4**	**15.5 ± 10.2**
χ = 27.7 µSI/g							
*JBL228Ta**	*3.7*	*23.2*	*807.3*	*449.5*	*0.029*	*122.1*	*19.0*
JBL228Tb	2.1	27.6	1418.0	22.0	0.019	10.3	12.2
χ = 17.7 µSI/g							
*JBL260Ta**	*2.8*	*16.4*	*543.1*	*424.0*	*0.030*	*154.0*	*26.4*
*JBL260Tb**	*6.0*	*7.1*	*68.3*	*493.4*	*0.105*	*81.8*	*57.6*
χ = 20.5 µSI/g							
JBL264Ta	5.7	31.8	728.3	34.7	0.044	6.1	18.4
JBL264Tb	12.5	18.0	145.0	66.1	0.124	5.3	11.4
Mean	**9.1 ± 4.8**	**24.9 ± 9.8**	**436.7 ± 412.5**	**50.4 ± 22.2**	**0.084 ± 0.057**	**5.7 ± 0.6**	**14.9 ± 4.9**

Because of this uncertainty, the noisy data were excluded from further analyses. This filtering yielded slightly more constrained ranges of the M_{rs}/M_s (0.005-0.171) and H_{cr}/H_c (2.13-149) ratios (Figure 4.9*a*).

Interestingly, while the thermomagnetic data indicated the presence of magnetite in almost all the samples, most of the magnetic hysteresis ratios plot off the SD-MD mixing lines predicted for pure magnetite (Dunlop, 2002). Most data points are shifted towards the SP-SD mixing line (Figure 4.9*a*) suggesting the presence of some amount of superparamagnetic (SP) grains. However, the shift can also reflect the presence of magnetically hard (high coercivity) mineral phases together with soft (low coercivity) minerals (Roberts et al., 2000).

In order to evaluate the potential correlation between the magnetic hysteresis properties and bulk mass-normalized magnetic susceptibility (χ) of the measured samples, the hysteresis data were categorized into three groups based on the corresponding values of χ. The thresholds at 50 μSI/g and 100 μSI/g were selected to split the entire range of χ (~0-145 μSI/g) into three approximately equal parts. No correlation between χ and magnetic hysteresis ratios have been noticed (Figures 4.9*a*, 4.10*a*, 4.11*a*).

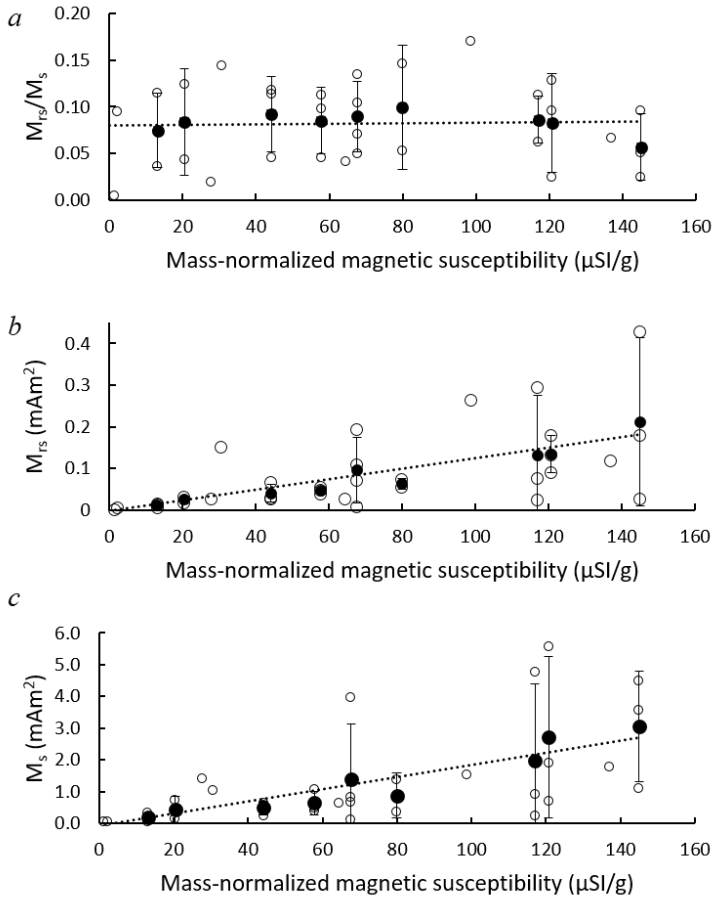

Figure 4.10 Dependences of *a*) the saturation remanence, M_{rs}, *b*) saturation magnetization, M_s, and *c*) the M_{rs}/M_s ratio on the mass-normalized magnetic susceptibility. Open circles show individual sample data and closed circles show sample-mean values (Table 1). The error bars are 1 σ. Dotted lines are the best-fit lines based on the individual data points.

However, an inverse correlation has been observed between χ and the amount of paramagnetic contribution to the total induced magnetic moment (Pearson's correlation coefficient R = -0.52) (Figure 4.9*b*). In addition, a positive correlation has been observed between χ and the values of saturation remanent magnetization, M_{rs} (R = 0.60) (Figure 4.10*b*) and saturation magnetization, M_s (R = 0.59) (Figure 4.10*c*). At the same time, the coercive force, H_c (R = 0.04) and coercivity of remanence (H_{cr}) (R = 0.16) show no correlation with χ (Figure 4.11*b*,*and c*).

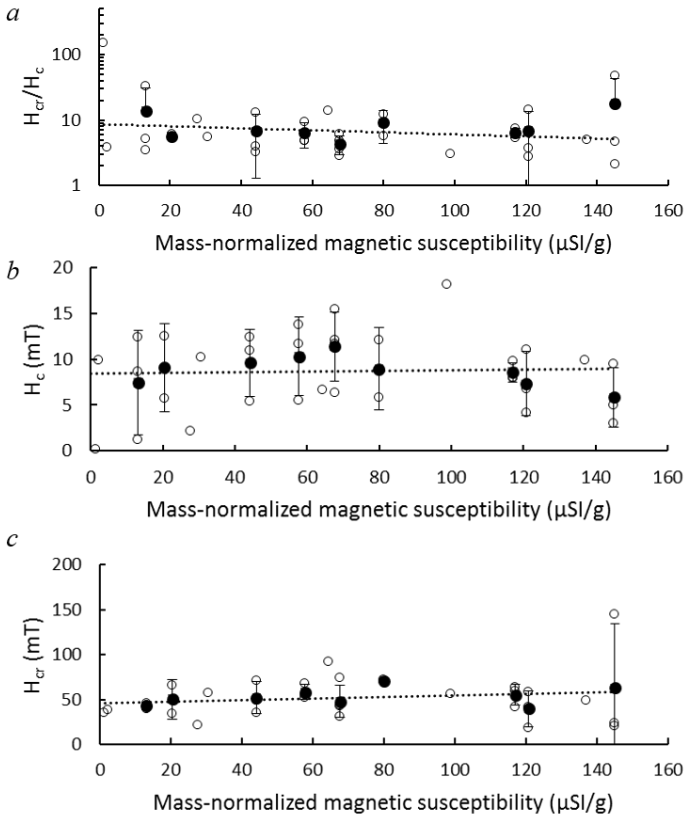

Figure 4.11. Dependences of *a*) the coercivity of remanence, H_{cr}, *b*) coercive force, H_c, and *c*) the H_{cr}/H_c ratio on the mass-normalized magnetic susceptibility. Open circles show individual sample data and closed circles show sample-mean values. The error bars are 1 σ. Dotted lines are the best-fit lines based on the individual data points.

4.5 Frequency Dependent Magnetic Susceptibility

In order to test for the presence of superparamagnetic grains suggested by the hysteresis data (Figure 4.9*a*), the dependence of low-field magnetic susceptibility on the measurement frequency was measured for the selected samples (Table 4.2). The measured κ_{fd}% ranged from 0.54% (a negligible frequency dependence) to 26% (a strong frequency dependence) (Table 4.2; Figure 4.12*a, and b*). The κ_{fd}% values also manifest a noticeable inverse correlation (R = -0.65) with the value of κ_{lf} measured at 976 Hz. The inverse relationship is best described by a power law $y = ax^b$ where a = 1.096 and b = -0.718 (Figure 4.12*c*).

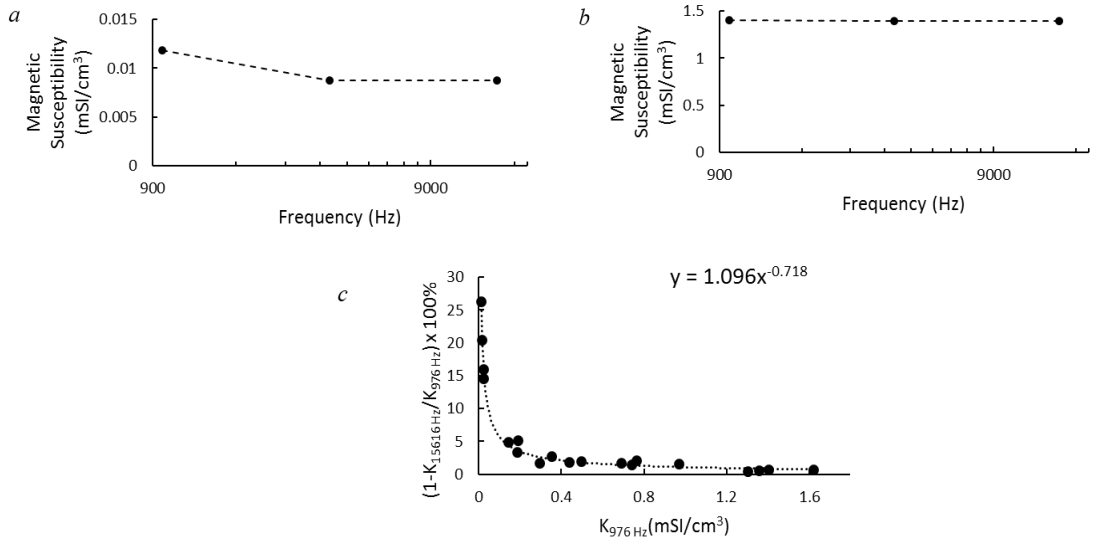

Figure 4.12 (*a, and b*) Examples of the frequency dependence of volume-normalized magnetic susceptibility (*K*) measured from samples characterized by a low (*a*) and high (*b*) values of *K*. *c*) The decrease of *K* measured at 15616 Hz ($K_{15616\ Hz}$) with respect to *K* measured at 976 Hz ($K_{976\ Hz}$) as a function of $K_{976\ Hz}$. Dotted curve shows the best-fit curve using a power function described by the equation $y = 1.096x^{-0.718}$.

Table 4.2 Volume-normalized magnetic susceptibility (K) measured at 976 Hz, 3904 Hz, and 15616 Hz frequencies. D is the relative difference between K_{976Hz} and $K_{15616Hz}$ [D(%) = (1-$K_{15616Hz}$/K_{976Hz}) x 100%].

Sample	K_{976Hz} (mSI/cm^3)	K_{3904Hz} (mSI/cm^3)	$K_{15616Hz}$ (mSI/cm^3)	D (%)
JBL15	1.358	1.345	1.350	0.59
JBL31	0.738	0.729	0.727	1.49
JBL37	0.016	0.013	0.013	20.41
JBL70	0.764	0.757	0.747	2.19
JBL71	0.021	0.018	0.017	16.06
JBL77	0.012	0.009	0.009	26.34
JBL105	1.622	1.600	1.610	0.74
JBL127	0.144	0.138	0.137	4.94
JBL137	1.405	1.397	1.395	0.71
JBL150	0.350	0.342	0.341	2.71
JBL185	0.970	0.958	0.954	1.67
JBL191	0.023	0.019	0.019	14.61
JBL192	0.689	0.685	0.677	1.76
JBL204	0.497	0.491	0.487	2.03
JBL207	0.438	0.435	0.429	1.94
JBL212	1.303	1.292	1.296	0.54
JBL228	0.296	0.289	0.291	1.73
JBL260	0.189	0.180	0.179	5.13
JBL264	0.186	0.180	0.179	3.44

4.6 Optical and Scanning Electron Microscopy

Upon initial inspection at low magnification all samples appeared to contain mostly quartz, and black angular and rounded grains, likely to be magnetite or titanomagnetite (Figure 4.13). There were other less frequent grains included such as occasional pyrite and possibly pyrrhotite, angular black grains and clay or silicate minerals (Figure 4.14). Increasing the magnification enabled the locating of small black spheres (~10µm in diameter) in multiple samples as well.

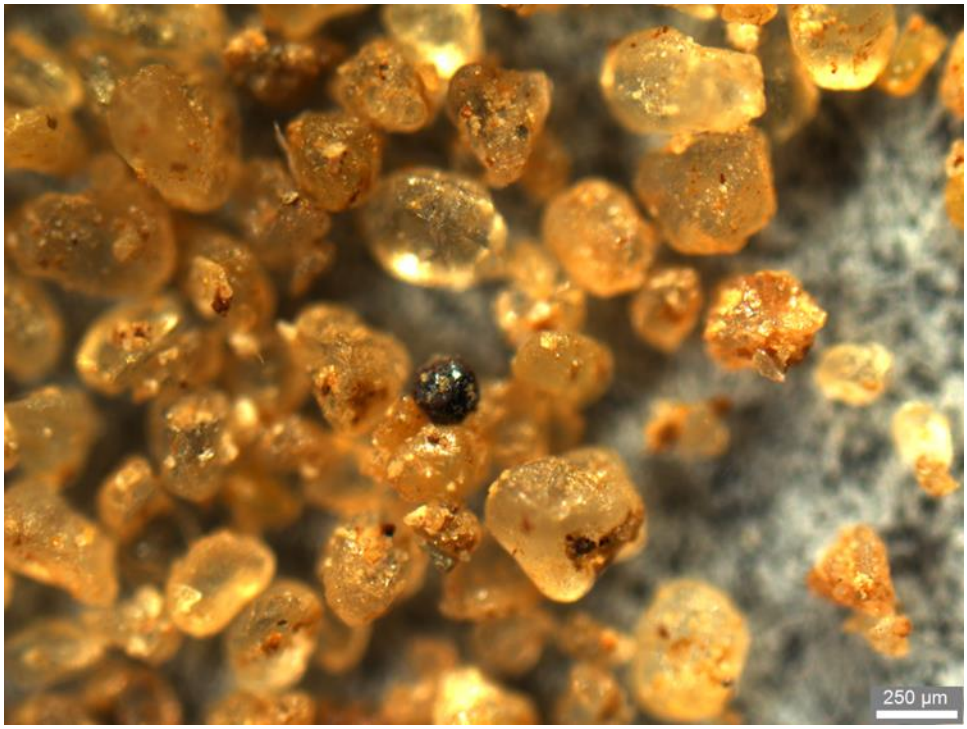

Figure 4.13 Photomicrograph of a round black grain located in sample JBL137 at four times magnification.

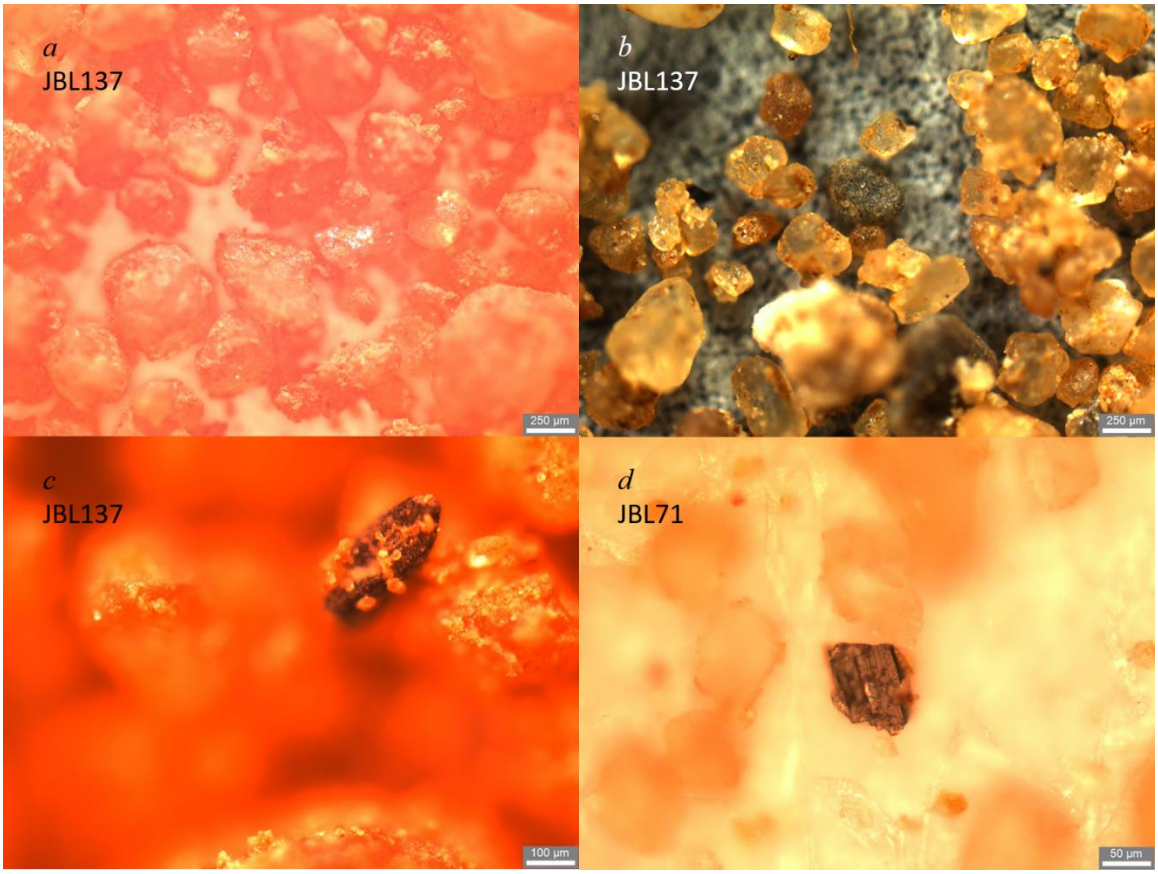

Figure 4.14 Photomicrographs of various minerals other than quarts located in samples. *a, b and c)* Photomicrographs of JBL137 displaying pyrite, pyrrhotite and angular black grains, respectively. *d)* A clay or silicate mineral in sample JBL71.

Scanning electron microscopy (SEM) was primarily used to identify the composition of the grains identified with the optical microscope. Using (XRD/EDS) the round and angular black grains were identified as iron oxides and titanium iron oxides (Figure 4.15). Unfortunately, locating the smaller (~10µm) spheres proved very difficult with the SEM and a composition could not be obtained.

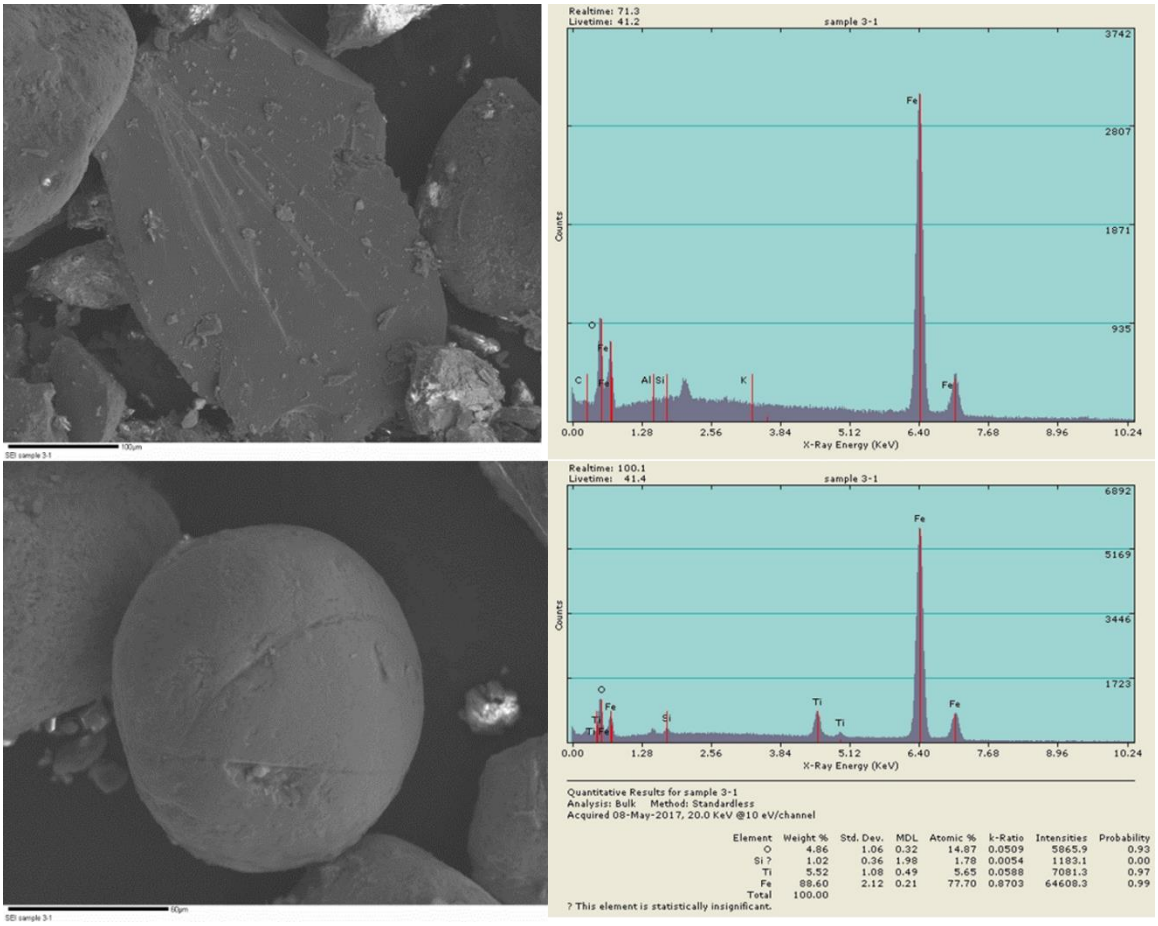

Figure 4.15 Scanning electron microscope image and spectra corresponding to grains observed in sample JBL105.

5.0 Discussion

5.1 Bulk Low-Field Magnetic Susceptibility as an Indicator of Hydrocarbon Reservoirs

The ultimate goal of this project was to investigate a potential relationship between the light hydrocarbon content and magnetic properties of the near-surface soils and sediments over the belt of Niagaran pinnacle reefs in the Lower Peninsula of Michigan. The working hypothesis was that light hydrocarbons migrate upwards and react with the authigenic

magnetic minerals in the near-surface soils and sediments thereby producing a different suite of magnetic minerals that can be distinguished by rock magnetic methods. This investigation primarily focused on the low-field magnetic susceptibility as a potential method for hydrocarbon exploration and environmental monitoring.

Unfortunately, data on the exact locations of the Niagaran pinnacle reefs obtained by exploration companies are not publicly available. Therefore we estimated the locations of hydrocarbon reservoirs based on the locations of wells producing oil, gas, or gas condensate available from a public domain database (http://www.michigan.gov/deq). The database allows categorizing the wells according to their type (e.g., gas, gas condensate, oil, dry, producing vs. abandoned, etc.), the target formation, and other parameters. The locations of wells (of all types) targeting the Niagaran Formation approximately delineate the extent of the reef belt in the sampled area (Figure 5.1). In our analyses, we also assumed that the locations of producing wells mark the hydrocarbon-bearing reef reservoirs (Figure 5.2). A drawback of this approach is that it does not allow distinguishing between individual reefs (two or more wells may represent the same reef).

The area of elevated magnetic susceptibility in the northeastern quadrant of the studied area lies within the reef belt and correlates with the locations of producing wells. However, at the same time, the high concentration of producing wells in the southwestern quadrant is not associated with elevated susceptibilities on the contour map. Therefore, at the large scale (i.e., larger than the typical extent of an individual reef, ~0.3-0.4 km), no correlation is observed between the presence of hydrocarbon reservoirs and elevated values of magnetic susceptibility in the near-surface sediments.

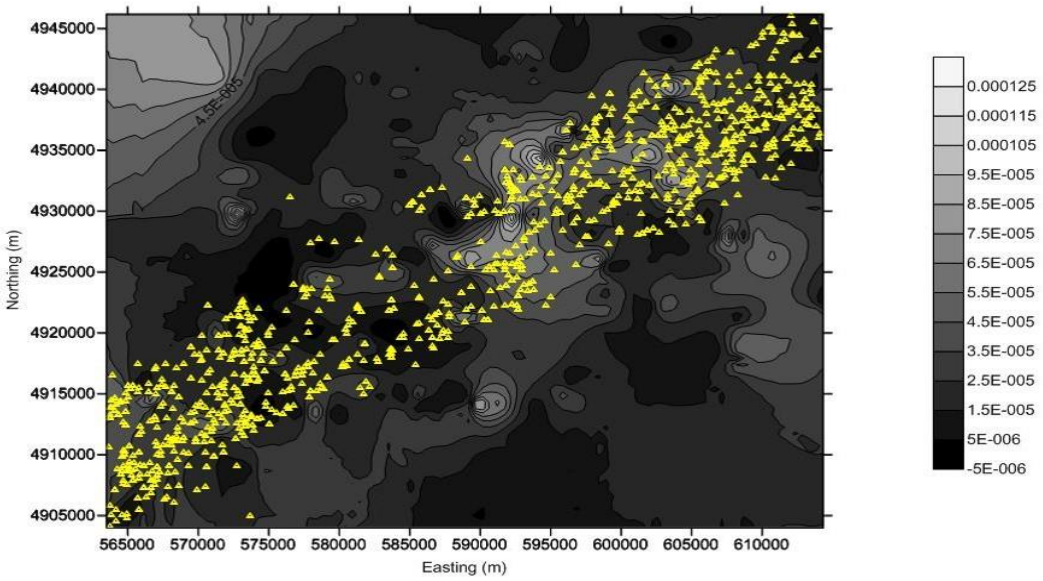

Figure 5.1 Locations of the wells (all types) with the Niagaran Formation as the target formation (yellow triangles). The locations delineate the trend and extent of the pinnacle reef belt.

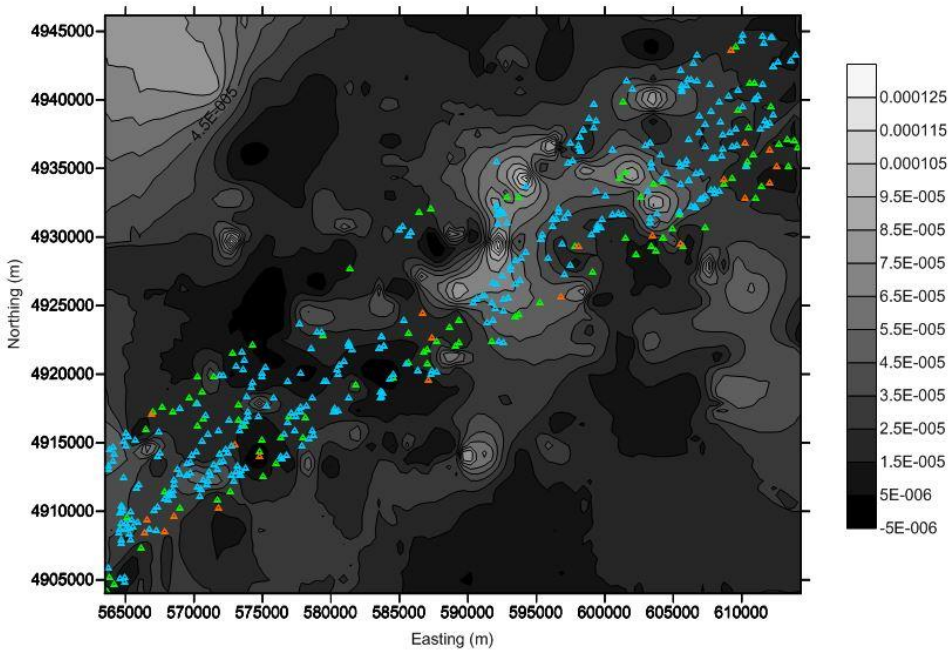

Figure 5.2 Locations of the producing wells that have the Niagaran Formation as their target formation. Green, blue and orange triangles represent gas, oil, and gas condensate wells, respectively.

Despite the lack of such a correlation, it is noteworthy that a smaller area of the elevated susceptibilities in the northwestern quadrant (centered at approximately 4930000N, 572500E) correlates with a cluster of producing gas wells representing the Devonian Traverse Group (Figure 5.3). This reservoir represents an entrapment of gas with a controversial source, but it suggested to have originated below the Niagaran reefs and migrated past them to accumulate in the younger, shallower Devonian rocks. It is significant that although elevated magnetic susceptibility does not show a straightforward correlation over the reef belt, it has indicated the only other producing area in the region.

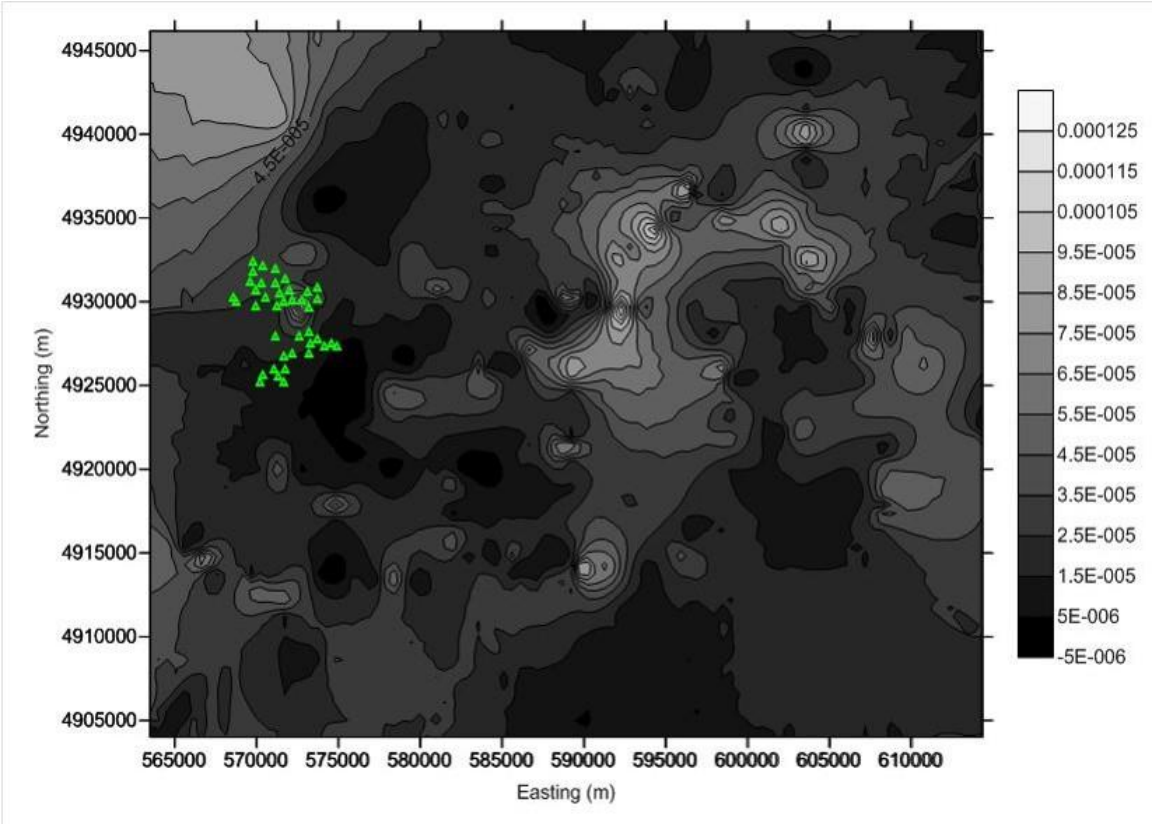

Figure 5.3 Correlation between the area of elevated magnetic susceptibility and locations of producing gas wells targeting the Devonian Traverse Group (cluster of green triangles).

The lack of a clear correlation between the hydrocarbon reservoirs and elevated values of susceptibility may also reflect a differential effect of hydrocarbons on rocks overlying different parts of the reef belt. For example, Machel and Burton (1991) concluded that the invasion of hydrocarbons may result in positive, absent, or negative magnetic contrasts, depending on the amounts of magnetite and pyrrhotite formed relative to the amounts of hematite destroyed. These amounts depend on a complex interplay of the sedimentological, chemical, microbiological, and hydrological conditions above and around the hydrocarbon accumulations. In this respect, it is noteworthy that the majority of lowest susceptibility values observed in this study were also obtained from the rocks overlying the reef belt (Figure 4.2b). The very low values may therefore reflect the effect of hematite dissolution without concurrent production of strong magnetic mineral phases (e.g., Kilgore and Elmore, 1989).

A second possible explanation for the trend of magnetic susceptibility observed over the reef may have to do with the flow of water within the area. Machel and Burton (1991) suggested that the ascension of microbubbles can be strongly affected by the local flow regime. Upon further investigation, it was discovered that there is some correlation between the uppermost glaciofluvial aquifer and the magnetic susceptibility trends observer in the region (Figure 5.4). Within this region the water table has a relatively consistent elevation (albeit a high elevation) with a steep decrease in the west-southwest direction. This indicates a relatively higher flow velocity in the southwest than in the northeast. It is, therefore possible that in the northeast, where the flow velocity would be lesser, the microbubbles were allowed to ascend and accumulate in the shallow subsurface.

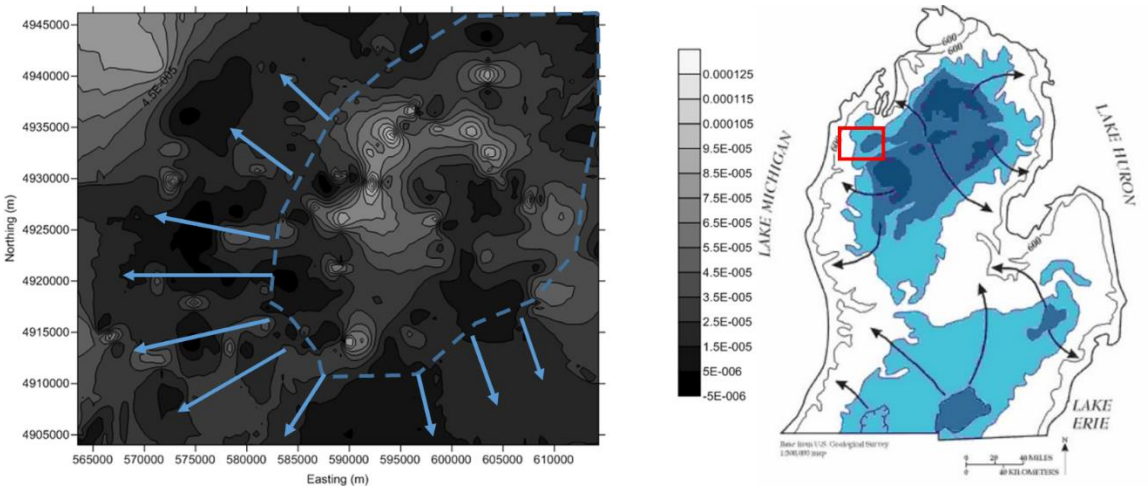

Figure 5.4 Map of water table elevations (right) and the approimate location within the study area (left). Dark blue represents water table elevations >1200ft., medium blue represents water table elevations >1000ft., light blue represents water table elevations >800ft. Arrows show approximate water flow directions.

Whereas, in the southwest, as the microbubbles reached the upper aquifer they were intercepted by the faster moving flow of groundwater and not allowed to accumulate. This is perhaps an unlikely mechanism to explain the pattern of magnetic susceptibility alone, however, it could be a contributing factor.

Our measurements show that both anomalously high and low values of magnetic susceptibility correlate with the hydrocarbon-bearing reef locations and may therefore represent the effect of hydrocarbon microseepage. However, because of the large variation and complexity of the magnetic susceptibility signal, it does not seem to be a straightforward indicator for a hydrocarbon reservoir within the reef belt. This conclusion is corroborated by an earlier investigation of a much smaller area near Bear Lake conducted by Kari Anderson in 2012 in which no correlation was observed between the known locations of the hydrocarbon-bearing reefs (and attendant geochemical anomalies; Seaman, 2002) and the values of low-field magnetic susceptibility.

However, on the other hand, the elevated susceptibility values observed outside the reef belt extent show a much better correlation with the presence of hydrocarbon reservoirs in the Devonian Traverse Group (Figure 5.3). Although the results from this project have not revealed a clear-cut relationship between hydrocarbon migration and elevated magnetic susceptibility, the correlation observed for the Devonian reservoirs indicates that the magnetic susceptibility method still represents a viable exploration approach, especially taking into account its cost and time efficiency. For example, while conventional (e.g. seismic) exploration efforts require long periods of data collection and processing, the sampling portion of this project in 2016 was completed in four days (~70 samples/day), bulk susceptibility measurements were completed in one week, and coordinate conversion and contouring (once the most suitable method was determined) required two days. This process totals approximately two weeks to produce a contour map of low-field magnetic susceptibility over a ~1200 km^2 area. Thus, if a definitive relationship can be shown, the magnetic susceptibility method may be a competitive option for exploration efforts because of the time saved to produce a map of elevated magnetic susceptibility.

5.2 Rock Magnetism

Another important question is what processes cause the observed enhancement of magnetic susceptibility and whether they are (or can be) related to hydrocarbon alteration. Thermomagnetic analyses indicate the presence of some amount of magnetite in practically all measured samples (including the background samples) independent of their bulk mass-normalized magnetic susceptibility, χ, measured at room temperature. This observation is

consistent with the presence of magnetite of detrital origin in all the investigated sediments that forms a natural "background" signal. However, the samples with higher bulk mass-normalized susceptibility contain more magnetite as is evidenced by typically stronger Verwey transitions observed in the initial (pre-heating) low-temperature κ(T) runs on these samples (e.g. Samples JBL105 and JBL212, Figures 4.4, 4.5). A notable exception of Sample JBL207 which yielded a moderate χ = 44.2 μSI/g but showed a strong Verwey transition (Figure 4.5) may reflect a significant heterogeneity of the sample. On the other hand, the initial low-temperature κ(T) curves measured from the samples with low initial magnetic susceptibility values are characterized by absent or weakly expressed Verwey transitions (e.g., Sample JBL 127, Figure 4.3). A similar difference in the expression of the Verwey transition between hydrocarbon-contaminated and unaffected sediments was previously reported by other authors (e.g., Rijal et al., 2012).

The initial low-temperature κ(T) curves measured from the low-susceptibility samples also exhibit a stronger paramagnetic decay at very low temperatures (e.g., Sample JBL37) while the high-susceptibility samples are typically dominated by a strong ferromagnetic signal (e.g., Sample JBL 105). Such a behavior is consistent with an overall decrease in the paramagnetic signal in the samples with higher χ indicated by magnetic hysteresis measurements (Figure 4.9*b*). The decrease in paramagnetic signal is mirrored by the decrease in the superparamagnetic contribution with increasing χ observed in the frequency-dependent susceptibility data (Figure 4.12*c*). These observations indicate that the new magnetite may have formed (at least, in part) at the expense of paramagnetic

minerals (e.g., siderite or clays) or ultrafine ferromagnetic particles, for example, as a result of iron(III)-reducing microorganism activity (e.g., Maher, 1998).

The increases of saturation magnetic moment (M_s) and saturation remanent magnetization (M_{rs}) with increasing χ (Figure 4.10*b, c*) are also consistent with the neoformation of magnetite associated with hydrocarbon migration observed in previous studies (e.g., Elmore et al., 1987). In many cases, the new magnetite is represented by nearly spherical particles sized from a few μm to several tens of μm in diameter (e.g., Elmore et al., 1987; Aldana et al., 2011; Guzmán et al., 2011). The presence of such larger pseudo-single-domain or multidomain grains may explain somewhat lower than average M_{rs}/M_s ratios observed for two samples with the highest susceptibility (Figure 4.10a). Furthermore, larger magnetite grains may also explain an apparent decrease in the coercivity (H_c) observed for the samples with high χ values (>80 μSI/g) (Figure 4.11*b*).

This interpretation is corroborated by the results of optical microscopy analyses in which the presence of large dark spheroidal grains was observed to be greater in samples with high bulk magnetic susceptibility than in those with low bulk magnetic susceptibility (Figure 5.4). The dark spheroids varied from tens of μm to 200-300 μm in size. Although identification of their mineralogy requires SEM and/or XRD analyses (underway), the previous publications and our rock magnetic data strongly suggest that they are magnetite spheres. Because samples were collected at depths of approximately one meter, it seems unlikely that the spheres have anthropogenic origin such as deeply buried fly ash, randomly dispersed throughout the field area, especially taking into account that the area is largely agricultural, devoid of fly ash producing industries.

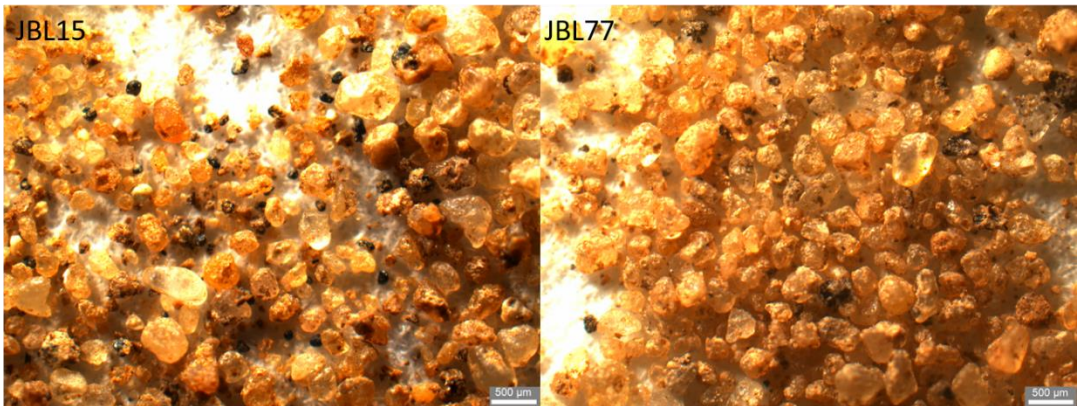

Figure 5.4 Photomicrographs of selected samples JBL15 and JBL77 displaying the difference in relative amounts of black spheroids in samples of differing magnetic susceptibility.

It was also observed that the spheroidal particles are magnetic as they moved in a gradient magnetic field created by a rare-earth magnet. Moreover, no spheroidal particles were observed in the sample with the lowest susceptibility (JBL77) and in the background sample (JBL264), consistent with the notion that the spheroidal particles are a product of hydrocarbon-related processes. Detrital magnetic particles, characterized by irregular shapes, were observed in all investigated samples. Importantly, additional optical microscopy observations performed on the samples characterized by medium-to-high bulk magnetic susceptibility values (Samples JBL15 and JBL127) also identified smaller spherical grains consistent with the dimensions (~5-15 μm) expected of hydrocarbon-induced magnetite particles (e.g., Elmore et al., Guzman et al., 2011) (Figure 5.5).

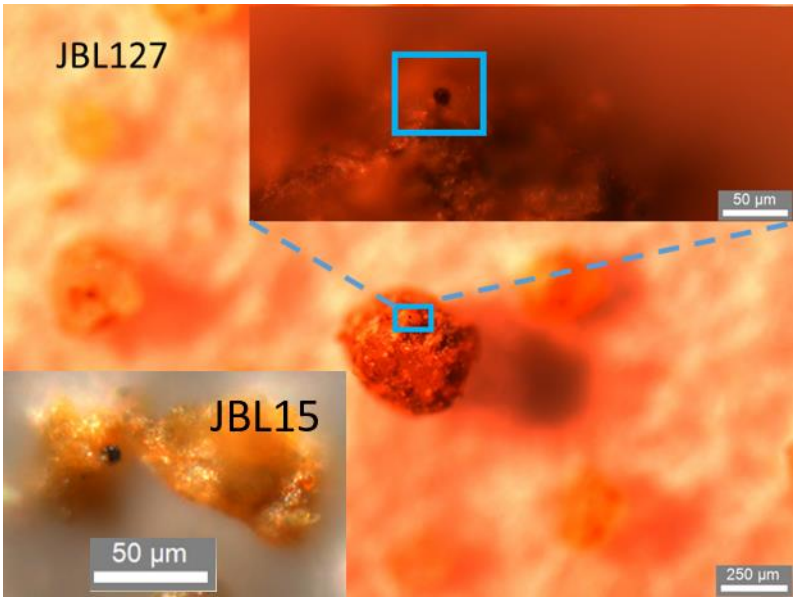

Figure 5.5 Photomicrographs of black spheres between 5-10 micron in diameter, occurring in samples JBL15 and JBL127 as growths on preexisting grains.

6.0 Conclusions

The present study has revealed that relationship between the hydrocarbon reservoirs and low-field magnetic susceptibility over the Niagaran pinnacle reef belt in the Michigan Basin is not straightforward. Both very high and very low susceptibility values have been observed within the extent of the reef belt in the studied area. The inverse relationship between increasing magnetic susceptibility and paramagnetic and superparamagnetic behavior implies chemical or microbial activity, as finer particles with higher surface area-to-volume ratios would be most vulnerable to bacterial consumption or chemical dissolution. However, this correlation is not straightforward within the areal extent of the reef belt. The lack of continuous correlation throughout the reef belt hampers definitive large-scale hydrocarbon detection, and may suggest other possible outcomes of

hydrocarbon-induced alteration of iron-bearing minerals in addition to elevated magnetic susceptibilities.

However, a good correlation with the Devonian hydrocarbon reservoirs outside of the belt indicates a potential of the surface magnetic susceptibility method for hydrocarbon detection at a smaller-scale. Additional field and laboratory investigations are needed to reveal the complex nature of the processes involved in the magnetic alteration of near-surface soils and sediments by microseepage of hydrocarbons. Future surveys may require multidisciplinary tests, such as investigation into the link between changes in the magnetic properties observed in this project and microbial content which may elucidate the specific processes involved in altering the magnetic minerals.

7.0 References

Abrams, M. A., 2005. Significance of Hydrocarbon Seepage Relative to Petroleum Generation and Entrapment. *Maine and Petroleum Geology*, 22, 457-477.

Aldana M., Costanzo-Alvarez V., Gomez L., Gonzalez C., Diaz M. Silva P. and Rada M., 2011. Identification of Magnetic Minerals Related to Hydrocarbon Authigenesis in Venezuelan Oil Fields Using an Alternative Decomposition of Isothermal Remanence Curves. *Stud Geophys Geod*, 55: 343.

Berger, Z., Davies, J., and Thompson, T.T., 2002. Integrated Analysis of High-Resolution Aeromagnetic (HRAM) and RADARSAT-1 Imagery for the Exploration in Mature and Frontier Basins. In: Schumacher, D., and LeSchack, L.A. (Eds.), Surface Exploration Case Histories: Application of Geochemistry, Magnetics, and Remote Sensing. AAPG Studies in Geology 48. *SEG Geophysical References Series*, 11, 345-360.

Briggs, J. C., 1974. Operation of Zoogeographic Barriers. *Systemic Zoology*. 23, 248-256.

Brown, A., 2000. Evaluation of possible gas microseepage mechanisms. *Association Petroleum Geochemical Exploration Bulletin*, 84, 1775–1789.

Chadima, M., and Hrouda, F., 2012. Thermomagnetic Curve Browser, Cureval 8.0.2 for Windows. Beta Version. AGICO, Inc., Brno, Czech Republic at www.agico.com.

Cohee, G. V., and Landes, K. K., 1958. Oil in the Michigan basin, In Weeks, L.G. (Ed.), Habitat in Oil. *American Association of Petroleum Geologists*, Tulsa, Oklahoma, 473-493. Coniglio, M., Zheng, Q., and Carter, T. R., 2003. Dolomitization and Recrystallization of Middle Silurian Reefs and Platformal Carbonates of the Guelph Formation, Michigan Basin, Southwestern Ontario. *Bulletin of Canadian Petroleum Geology*, 51, 177-199.

Davis, J. C., 1986. *Statistics and Data Analysis in Geology*, Wiley, New York, 639 pp.

Day, R., Fuller, M., and Schmidt V. A., 1977. Hysteresis Properties of Titanomagnetites: Grain- Size and Compositional Dependence, *Physics of the Earth and Planetary Interiors*, 13, 260– 267.

Donovan, T. J., Forgey, R. L., and Roberts, A. A., 1979. Aeromagnetic Detection of Diagenetic Magnetite over Oil Fields. *American Association of Petroleum Geologists Bulletin*, 63, 245– 248.

Dunlop, D. J., and Özdemir, Ö, 1997. *Rock Magnetism: Fundamentals and Frontiers*, Cambridge University Press, New York, 573 pp.

Dunlop, D. J., 2002. Theory and Application of the Day plot (Mrs/Ms versus Hcr/Hc): 1. Theoretical Curves and Tests Using Titanomagnetite Data, *Journal of Geophysical Research*, 107, 2056, doi:10.1029/2001JB000486.

Ellwood, B. B., and Burkart, B., 1996. Test of Hydrocarbon-Induced Magnetic Patterns in Soils: The Sanitary Landfill as Laboratory. In: Schumacher, D., Abrams, M.A. (Eds.), Hydrocarbon Migration and Its Near-Surface Expression. *American Association of Petroleum Geologists Memoirs*, 66, 91–98.

Elmore, R. D., Engel, M. H., Crawford, L., Imbus, S., and Sofer, Z., 1987. Evidence for a Relationship Between Hydrocarbon and Authigenic Magnetite. *Nature*, 325, 428–430.

Elmore, R. D., and Crawford, L., 1990. Remanence in authigenic magnetite: testing the hydrocarbon–magnetite hypothesis. *Journal of Geophysical Research*, 95, 4539–4549.

Elmore, R. D., Scott, W. I., Engel, M. H., and Fruit, D., 1993. Hydrocarbon and Magnetization in Magnetite. *SEPM Special Publication 49*, 181-191.

Foote, R. S., 1987. Correlations of Borehole Rock Magnetic Properties with Oil and Gas Producing Areas. *Association of Petroleum Geochemical Explorationists Bulletin*, 3, 114-134.

Foote, R. S., and Long, G. J., 1988. Correction of Oil and Gas Producing Areas with Magnetic Properties of the Upper Rock Column, Eastern Colorado. *Association of Petroleum Geochemical Explorationists Bulletin*, 4, 47-61.

Foote, R. S., 1996. Relationship of Near-Surface Magnetic Anomalies to Oil- and Gas-Producing Areas, In: Schumacher, D., Abrams, M.A. (Eds.), Hydrocarbon Migration and Its Near- Surface Expression. *American Association of Petroleum Geologists Memoirs*, 66, 111–126.

Friedman, G. M., and Kopaska-Merkel, D. C., 1991. Late Silurian Pinnacle Reefs of Northern Michigan. In: Catacosinos, P. A., Daniels, P. A. Jr. (Eds.), Early Sedimentary Evolution of the Michigan Basin. *Geological Society of America Special Paper 256*, 89-100.

Gill, D., 1979. Differential Entrapment of Oil and Gas in Niagaran Pinnacle-Reef Belt of Northern Michigan. *American Association of Petroleum Geologists Bulletin*, 63, 608-620.

Goldhaber, M. B., and Reynolds, R. L., 1991. Relations Among Hydrocarbon Reservoirs, Epigenetic Sulfidization, and Rock Magnetization: Examples From the South Texas Coastal Plain. *Geophysics*, 56, 748–757.

Guzman O., Costanzo-Alvarez V., Aldana M. and Diaz M., 2011. Study of Magnetic Contrasts applied to Hydrocarbon Exploration in the Maturin Sub-Basin (eastern Venezuela). Stud. Geophys. Geod., 55, 359-376.

Henry, W. E., 1988. Magnetic Detection of Hydrocarbon Microseepage in a Frontier Exploration Region. *Association of Petroleum Geochemical Explorationists Bulletin*, 4, 18–29.

Hughes, L. J., Zonge K. L., and Carlson, N. R., 1986. The application of electrical techniques in mapping hydrocarbon-related alteration. In: Davidson, M. J. (Ed), Unconventional methods
in exploration for petroleum and natural gas, symposium IV: Dallas, Texas, Southern Methodist University Press, 5–26.

Klusman, R. W., 1993. *Soil Gas and Related Methods for Natural Resource Exploration*, Chichester, John Wiley and Sons, 483 pp.

Klusman, R. W., and Saeed, M. A., 1996. Comparison of light hydrocarbon microseepage mechanisms. In: Schumacher, D., Abrams, M.A. (Eds.), Hydrocarbon Migration and Its Near-Surface Expression. *American Association of Petroleum Geologists Memoirs* 1996, 66, 157-168.

Krs, M., Novak, F., Krsova, M., Pruner, P., Kouka-Likova, L., and Jansa, J., 1992. Magnetic Properties and Metastability of Greigite-Smythite Mineralization in Brown-Coal Basins of the Krusne Lory Piedmont. *Bohemia. Phys. Earth Planet. Inter*, 70, 273-287.

Liu, Q. S., Chan, L. S., Liu, Q. S., Li, H. X., Wang, F., Zhang, S. X., Xia, X. H., and Cheng, T.J., 2004. A Study of Relationship Between Magnetic, Geochemical and Mineralogical Anomalies and Hydrocarbon Microseepage Above Oil and Gas Field, Ordos Basin in China. *American Association of Petroleum Geologists Bulletin*, 88, 241–251.

Machel, H. G., and Burton, E. A., 1991. Causes and Spatial Distribution of Anomalous Magnetization in Hydrocarbon Seepage Environments. *American Association of Petroleum Geologists Bulletin*, 75, 1864–1876.

Machel, H. G., 2001. Bacterial and Thermochemical Sulfate Reduction in Diagenetic Settings - Old and New Insights. *Sedimentary Geology*, 140, 143–175.

Madhavi, T., Kalpana, M.S., Patil, D.J., and Dayal, A.M., 2011. Evidence for a Relationship Between Hydrocarbon Microseepage and Trace Metal Anomalies: An Implication for Petroleum Exploration. *Geoscience Journal*, 15, 197-206.

Maher, B. A. 1988. Magnetic Properties of Some Synthetic Sub-Micron Magnetics. *Geophysical Journal International*, 94, 83-96.

Maher B.A., 1998. Magnetic Properties of Modern Soils and Quarrternary Loessic Paleosols: Paleoclimatic Implications. Palaeogeogr. Palaeoclimatol. Palaeoecol., 137, 25-54.

Mantek, W., 1973. Niagaran Pinnacle Reefs in Michigan, in: Geology in the Environment: Man, Earth, and Nature in Northwestern Lower Michigan. *Michigan Basin Geological Society*, Annual Field Excursion. 35-46.

McCabe, C., and Elmore, R. D., 1989. The Occurrence and Origin of Late Paleozoic Remagnetization in The Sedimentary Rocks of North America. *Reviews of Geophysics*, 27, 471–494.

McCabe, C., Sassen, R., and Saffer, B., 1987. Occurrence of Secondary Magnetite within Biodegraded Oil. *Geology*, 15, 1351–1370.

Oehler, D. Z., and Sternberg, B. K. 1984 Seepage-induced anomalies, "false" anomalies, and implications for electrical prospecting: -*American Association of Petroleum Geologists Bulletin*, 68, 1121–1145.

Price, L. C. 1986. A critical overview and proposed working model of surface geochemical exploration. In: Davidson, M. J. (Ed.), *Unconventional methods in exploration for petroleum and natural gas*, symposium IV: Dallas, Texas, Southern Methodist University Press, 245– 304.

Reynolds, R. L., Fishman, N. S., Wanty, R. B., and Goldhaber, M. B., 1990a. Iron Sulfide Minerals at Cement Oil Field, Oklahoma: Implications for Magnetic Detection of Oil Fields. *Geological Society of America Bulletin*, 102, 368–380.

Reynolds, R. L., Webring, M., Grauch, V. J. S., and Tuttle, M. L., 1990b. Magnetic Forward Models of Cement Oil Field, Oklahoma. Based on Rock Magnetic, Geochemical, and Petrologic Constraints. *Geophysics*, 55, 344–353.

Reynolds, R. L., Sweetkind, D. S., Axford, Y., 2001. An Inexpensive Magnetic Mineral Separator for Fine-Grained Sediment, *Open-File Report 01-281*, U.S. Geological Survey, Denver, Colorado, 7 pp.

Rijal, M. L., Porsch K., Appel E. and Kappler A., 2012. Magnetic Signature of Hydrocarbon-Contaminated Soils and Sediments at the Former Oil Field Hanigsen, Germany, Stud. Geophys. Geod., 56, 889-908.

Roberts, A. P., Pike, C. R., and Verosub, K. L., 2000. First-Order Reversal Curve Diagrams: A New Tool for Characterizing the Magnetic Properties of Natural Samples. *Journal of Geophysical Research*, 105, 28,461–28,475.

Sassen, R., McCabe, C., Kyle, J. R., and Chinn, E. W., 1989. Deposition of Magnetic Pyrrhotite During Alteration of Crude Oil And Reduction of Sulfate. *Organic Geochemistry*, 14, 381– 392.

Saunders, D. F., Burson, K. R., and Thompson, C. K., 1991. Observed Relation of Soil Magnetic Susceptibility and Soil Gas Hydrocarbon Analysis to Subsurface Hydrocarbon Accumulation. *American Association of Petroleum Geologists Bulletin*, 75, 389–408.

Saunders, D., Burson, K. R., and Thompson, C. K., 1999. Model for hydrocarbon microseepage and related near-surface alterations. *Association Petroleum Geochemical Exploration Bulletin*, 83, 170–185.

Schumacher, D., 1996. Hydrocarbon-Induced Alteration of Soils and Sediments. In: Schumacher, D. and M. A. Abrams (Eds.), Hydrocarbon migration and its near surface expression. *American Association of Petroleum Geologists Memoirs,* 66, 71–89.

Schumacher, D., 2009. Non-seismic Detection of Hydrocarbons: An Overview. Adapted from poster.

Scotese, C., Bambach, R. K., Barton, C., Van der Voo, R., and Ziegler, A., 1979. Paleozoic Base Maps: *Journal of Geology*, 7, 299-302.

Seaman, C. C., 2002. *Application of Solid-Phase Microextraction Technology in Surface Geochemical Exploration,* M.S. thesis, Michigan Technological University, Houghton, 72 pp.

Thompson, C. K., Saunders, D. F., and Burson, K. R., 1994. Model advanced for hydrocarbon microseepage, related alterations. *Oil and Gas Journal*, 14, 95–99.
Tompkins, K., 1990. Direct Location Techniques: Unified Theory. *Oil and Gas Journal*, 24, 126- 134.

Tompkins, K., 1990. Direct Location Technologies: Unified Theory. *Oil Gas Journal*. 88, 126-134.

Verwey, E. J. W., 1939. Electron Conduction of Magnetite (Fe3O4) and its Transition Point at Low Temperatures. *Nature*, 144, 327-328.

8.0 Appendices

Table 8.1 Mass-normalized magnetic susceptibility data incorporated in contour map (Figure 4.2). * Indicates samples included in rock magnetic investigation.

Sample	Easting	Northing	X (mass normalized)	Sample	Easting	Northing	X (mass normalized)
1	599643.239	4917680	1.48033E-05	46	571345.834	4920056	4.8293E-05
2	599054.948	4917085	2.30392E-05	47	572495.849	4920037	1.46123E-06
3	598400.647	4916458	1.35541E-05	48	573624.115	4919988	7.64472E-06
4	597900.165	4915895	1.88586E-05	49	574198.958	4919995	1.25425E-05
5	597306.028	4915670	1.97657E-05	50	575769.084	4919982	9.14277E-06
6	596580.923	4915320	2.42177E-05	51	576831.796	4919871	1.10921E-05
7	595833.161	4915000	4.33643E-05	52	578026.101	4919854	3.7573E-07
8	595150.363	4914774	2.44574E-05	53	579021.426	4919836	9.23479E-06
9	594424.602	4914455	1.57638E-05	54	580190.604	4920066	1.43571E-05
10	593743.032	4914137	9.18494E-06	55	581274.349	4920049	5.64597E-07
11	592925.534	4914032	2.35671E-05	56	582317.395	4919753	3.03363E-06
12	592216.051	4914115	4.18887E-05	57	583422.923	4919767	1.14409E-06
13	591397.235	4914103	7.30473E-05	58	584727.846	4919753	4.31864E-07
14	590577.991	4914123	5.56436E-05	59	585811.676	4919736	1.7117E-05
*15	589825.57	4914112	0.000116973	60	586696.107	4919748	4.5639E-06
16	589230.59	4913919	2.949E-05	61	588885.073	4919778	2.26067E-05
17	589106.229	4913300	4.11454E-05	62	589205.607	4918980	1.2113E-05
18	588310.285	4913227	5.92572E-05	63	589199.117	4917838	2.11895E-05
19	587558.178	4913186	3.96263E-05	64	589193.46	4916634	3.10619E-05
20	587358.568	4913215	1.46543E-05	65	589207.807	4915585	1.67968E-05
21	586007.643	4913258	2.9664E-05	66	589200.024	4914536	1.28153E-05
22	585276.86	4913280	1.7412E-05	67	574857.531	4914633	1.34157E-06
23	584479.685	4913300	3.11463E-05	68	574866.556	4915775	1.36289E-05
24	583728.365	4913198	3.16206E-05	69	574854.514	4916824	4.24842E-06
25	583063.202	4913282	3.19079E-05	*70	574842.116	4917904	6.44126E-05
26	582996.805	4913281	1.54741E-05	*71	574829.007	4919046	1.2955E-06
27	582199.645	4913302	1.7402E-05	72	574815.541	4920218	1.1052E-05
28	580693.495	4913376	1.85537E-05	73	575450.615	4920750	1.49235E-06
29	579940.247	4913428	1.54637E-06	74	576196.833	4921221	1.37012E-06
30	579254.908	4913358	1.48784E-05	75	576382.747	4922335	1.81133E-05
*31	578146.824	4913468	6.76279E-05	76	576414.632	4923384	9.15891E-07
32	577593.899	4913431	1.69804E-05	*77	576423.318	4924526	8.60656E-07
33	576840.328	4913514	1.89986E-06	78	576431.994	4925668	1.05606E-06
34	576022.183	4913443	2.39417E-05	79	576440.661	4926810	5.94899E-06
35	575246.862	4913496	9.63386E-07	80	576010.915	4927669	1.51302E-06
36	574494.04	4913518	2.88647E-06	81	575976.924	4928687	1.83807E-05
*37	573763.007	4913571	1.0795E-06	82	598800.531	4919272	1.5602E-05
38	572943.465	4913624	3.36293E-05	83	598876.338	4920107	1.42915E-05
39	571371.492	4913668	2.5913E-05	84	598886.268	4920909	2.73677E-05
40	570574.452	4913690	1.82935E-05	85	598805.899	4921834	4.41912E-05
41	569799.55	4913713	3.90477E-06	86	598835.583	4922791	2.32315E-05
42	569002.851	4913704	4.45832E-05	87	598820.588	4923779	2.35152E-05
43	568294.351	4913728	3.57127E-05	88	598850.249	4924736	2.93098E-05
44	567563.409	4913782	1.38596E-05	89	598815.027	4925599	2.30169E-05
45	570283.934	4920106	1.34823E-05	90	598822.58	4926556	4.16197E-05

Table 8.1 (Cont'd)

Sample	Easting	Northing	X (mass normalized)	Sample	Easting	Northing	X (mass normalized)
91	598785.484	4927543	2.55142E-05	**136**	573107.075	4930567	3.84701E-05
92	598771.412	4928469	2.05778E-05	***137**	573051.268	4929641	0.000137218
93	602776.135	4929426	1.59161E-05	**138**	576446.829	4926285	1.31104E-06
94	602553.886	4929515	1.73086E-05	**139**	577551.971	4926237	1.35962E-05
95	601757.13	4929626	1.21564E-05	**140**	578479.68	4926248	3.88969E-06
96	600630.674	4929639	2.6753E-05	**141**	579450.813	4926321	2.82405E-07
97	599703.877	4929594	1.97366E-05	**142**	580445.16	4926303	2.30336E-05
98	598775.663	4929642	3.63954E-05	**143**	581395.34	4926284	1.60241E-05
99	597871.405	4929566	2.3359E-05	**144**	582256.785	4926295	2.14394E-05
100	596987.825	4929584	1.4546E-05	**145**	583141.108	4926244	9.11848E-07
101	595994.32	4929569	2.80844E-05	**146**	584047.935	4926163	1.12579E-05
102	595045.423	4929524	4.53581E-05	**147**	584953.175	4926206	1.12659E-05
103	594139.332	4929573	2.80022E-05	**148**	585877.235	4926496	1.67463E-06
104	593168.353	4929528	4.18864E-05	**149**	586509.979	4927090	7.26349E-05
***105**	592218.567	4929545	0.000145307	***150**	587340.947	4927719	3.05588E-05
106	591247.146	4929531	2.95444E-05	**151**	587795.115	4928435	3.96689E-06
107	590556.28	4929985	6.73917E-06	**152**	588246.248	4929367	2.56387E-06
108	589713.123	4930282	7.00656E-05	**153**	588611.472	4930112	5.93576E-05
109	588764.314	4930238	7.62141E-05	**154**	589152.723	4929286	1.48005E-05
110	587881.304	4930226	1.80585E-06	**155**	589142.499	4928422	3.12781E-05
111	586997.882	4930245	8.92753E-07	**156**	589155.622	4927466	4.56145E-05
112	586026.168	4930263	1.88641E-05	**157**	589168.32	4926540	8.06185E-05
113	585165.242	4930251	1.43096E-05	**158**	589182.286	4925522	7.95696E-05
114	584171.466	4930269	3.29357E-05	**159**	589197.095	4924442	1.33167E-05
115	583311.336	4930196	1.85814E-05	**160**	589185.15	4923701	2.29687E-05
116	582295.49	4930214	2.90472E-05	**161**	589221.207	4922683	1.49997E-05
117	581412.102	4930234	2.00123E-05	**162**	589190.109	4921726	1.0165E-05
118	580798.612	4929856	7.29081E-06	**163**	589201.944	4920862	1.93536E-05
119	580892.297	4929425	8.45967E-06	**164**	589194.202	4919813	2.22748E-05
120	579855.027	4929381	1.80213E-05	**165**	608358.865	4916431	2.41847E-05
121	578971.167	4929432	2.19514E-05	**166**	608322.389	4917294	5.73447E-05
122	578065.618	4929452	1.34861E-05	**167**	608288.48	4918004	7.25418E-06
123	577093.845	4929471	2.26282E-05	**168**	608347.652	4918437	5.99837E-05
124	576122.444	4929460	1.65666E-05	**169**	608353.864	4919394	4.57843E-05
125	575217.274	4929449	7.92219E-06	**170**	608338.982	4920288	4.26743E-05
126	574267.243	4929500	2.44259E-05	**171**	608278.859	4921244	2.60316E-06
***127**	573340.005	4929490	1.31432E-05	**172**	607979.699	4921949	2.6199E-05
128	572347.911	4929355	6.13945E-05	**173**	607523.85	4922775	3.14437E-05
129	571462.434	4929561	2.15394E-05	**174**	606983.773	4923352	3.63546E-05
130	573726.092	4936314	1.3164E-06	**175**	607057.448	4924248	4.67779E-05
131	573099.055	4935196	8.84179E-06	**176**	606801.214	4925047	1.75489E-05
132	573130.856	4934332	8.61032E-06	**177**	606763.415	4926003	2.32822E-05
133	573074.755	4933437	4.2325E-05	**178**	606835.55	4926992	4.54639E-05
134	573086.225	4932418	4.22376E-05	**179**	606688.843	4927853	1.82732E-05
135	573075.275	4931431	1.40256E-05	**180**	606804.103	4928905	2.2328E-05

Table 8.1 (Cont'd)

Sample	Easting	Northing	X (mass normalized)	Sample	Easting	Northing	X (mass normalized)
181	606833.546	4929800	2.23861E-05	**226**	584374.9168	4936691	9.90164E-06
182	603610.204	4929748	7.80636E-06	**227**	584384.1093	4937678	1.84459E-05
183	603596.42	4930612	5.96219E-05	***228**	584373.6584	4938481	2.77026E-05
184	603559.085	4931568	4.42597E-05	**229**	584316.3045	4939498	3.75321E-05
***185**	603610.52	4932495	9.866E-05	**230**	584371.1737	4940363	2.02645E-05
186	603685.479	4933329	6.16702E-05	**231**	584336.2654	4941350	2.59085E-05
187	603943.148	4935154	3.50641E-05	**232**	585390.7936	4941611	1.16762E-05
188	603533.267	4935950	4.62796E-05	**233**	586272.2484	4941623	2.39555E-05
189	603540.534	4936876	2.15338E-05	**234**	587241.4327	4941667	1.80599E-05
190	603503.691	4937801	2.3882E-05	**235**	588096.646	4941987	2.14576E-05
***191**	603466.36	4938758	2.20504E-06	**236**	588908.1318	4942276	2.3491E-05
***192**	603454.035	4939529	7.9907E-05	**237**	589853.0344	4942474	2.41057E-05
193	603437.763	4940547	8.19175E-05	**238**	590800.914	4942456	5.46572E-06
194	603444.02	4941535	1.66143E-05	**239**	591857.2201	4942564	8.6657E-06
195	603386.137	4942398	3.53889E-05	**240**	592321.2432	4942478	2.75262E-06
196	603416.885	4943232	1.87984E-06	**241**	593181.0039	4942459	1.5482E-05
197	603400.6	4944250	9.0792E-07	**242**	594106.4263	4942473	3.36707E-05
198	603408.806	4945115	1.33886E-05	**243**	595075.9161	4942487	1.08754E-05
199	603414.04	4946164	3.27952E-05	**244**	596045.4059	4942501	7.13722E-06
200	598781.781	4930691	2.21618E-05	**245**	598262.3833	4941639	2.33603E-05
201	598787.888	4931741	2.82462E-05	**246**	583285.2296	4940812	1.90491E-05
202	598773.797	4932666	4.43236E-05	**247**	582359.1996	4940831	8.32333E-06
203	598780.36	4933685	4.77184E-05	**248**	581345.0226	4940849	3.394E-05
***204**	598744.67	4934579	5.77553E-05	**249**	580485.8932	4940807	1.38332E-05
205	598799.099	4935352	4.51716E-05	**250**	579493.0526	4942678	1.93418E-05
206	598765.286	4936123	2.54934E-05	**251**	578611.4635	4940877	7.67597E-06
***207**	597658.315	4936384	4.41452E-05	**252**	577553.9821	4940833	1.58834E-05
208	596795.414	4936556	8.62997E-06	**253**	576649.6655	4940884	2.46798E-05
209	596158.132	4936392	9.48531E-05	**254**	575701.29	4940935	2.29639E-05
210	595706.83	4935583	3.55871E-05	**255**	574644.1653	4940861	1.38197E-05
211	595054.607	4934925	2.79418E-05	**256**	573828.3908	4940882	3.7846E-05
***212**	594268.535	4934358	0.000120693	**257**	572615.9349	4940899	5.1134E-05
213	593526.899	4933761	8.4969E-05	**258**	571579.1131	4940980	8.32255E-05
214	592828.373	4933226	4.63815E-05	**259**	590525.7491	4945550	6.48938E-06
215	592020.273	4932629	8.62154E-05	**260**	590545.6348	4944602	8.41755E-06
216	591321.936	4932063	6.02899E-05	**261**	590567.7491	4943684	1.53336E-05
217	590534.333	4931558	2.43242E-05	**262**	590583.9287	4942623	3.73653E-06
218	589746.609	4931054	2.82725E-05	**263**	591297.3285	4942479	2.05362E-05
219	589177.386	4930706	2.89252E-05	**264**	592175.9274	4942808	2.90273E-05
220	584334.436	4931321	1.95975E-05	**265**	592765.1976	4942470	5.01633E-05
221	584344.878	4932216	2.58859E-05	**266**	593800.2847	4941669	9.98031E-06
222	584332.445	4933172	1.1138E-05	**267**	593788.3849	4941669	8.11068E-06
223	584476.853	4933945	2.26221E-05	**268**	593806.9502	4940662	3.36828E-05
224	584443.941	4934778	1.97455E-05	**269**	593850.9541	4939816	1.02599E-05
225	584365.314	4935734	3.99857E-05	**270**	594334.5515	4939219	2.31455E-05

Table 8.1 (Cont'd)

Sample	Easting	Northing	X (mass normalized)	Sample	Easting	Northing	X (mass normalized)
271	595239.3	4939233	3.0395E-05	**316**	593561.3	4929535	3.50821E-05
272	595880.4	4937568	3.3834E-05	**317**	592151.3	4942495	2.27981E-05
273	596361.6	4936979	9.90532E-05	**318**	591245.8	4929502	5.51351E-05
274	597177.3	4936512	1.4436E-05	**319**	590486.6	4930073	3.6458E-06
275	598022.3	4936295	4.07988E-06	**320**	589750	4930264	8.05001E-06
276	598994.9	4935793	3.40206E-05	**321**	587882.3	4930248	1.704E-05
277	598712.3	4935139	9.94625E-05	**322**	586960.3	4930245	2.02513E-05
278	601951.8	4934466	9.06867E-05	**323**	585929.6	4930251	1.52053E-05
279	601971	4933243	3.86045E-05	**324**	584359.8	4932799	1.11164E-05
280	601974.6	4932173	4.2401E-05	**325**	584513.7	4934201	2.85376E-05
281	601990	4931195	2.00283E-05	**326**	584396.1	4935199	2.06066E-05
282	602786.7	4931243	5.03696E-05	**327**	584366.8	4935927	2.68307E-05
283	603874	4931258	5.21217E-05	**328**	584380.2	4937028	3.90329E-06
284	604654.2	4931263	6.17976E-05	**329**	584387.6	4937986	2.23434E-05
285	605268.5	4930470	1.64196E-05	**330**	584397.7	4938836	8.1335E-06
286	605045.6	4929668	4.88044E-05	**331**	577155.2	4932667	1.47323E-05
287	606095.2	4929657	5.38241E-06	**332**	578078.3	4932654	1.0238E-05
288	606777.9	4928185	2.0412E-05	**333**	579088.9	4932634	3.62714E-05
289	607631.3	4927953	0.000101948	**334**	580196.2	4932611	2.59338E-05
290	608407.9	4927958	4.49476E-06	**335**	581142.6	4931591	2.44902E-05
291	609683.7	4927995	6.15545E-05	**336**	581131.3	4930688	6.12574E-05
292	610409.9	4928000	3.52216E-05	**337**	581124.2	4929771	1.78221E-05
293	610812.7	4927779	3.9867E-05	**338**	581131.7	4928747	6.53918E-06
294	610819.5	4926369	5.85966E-05	**339**	581121.9	4927836	1.17591E-05
295	598792.4	4927870	4.33935E-05	**340**	582405.8	4927852	2.37339E-05
296	598812.9	4925830	3.60328E-05	**341**	582761.6	4927799	2.15069E-05
297	598808.9	4925829	0.000100816	**342**	582982.5	4926902	2.05954E-05
298	598833.2	4924930	1.75256E-05	**343**	583181.9	4926233	7.74929E-05
299	598840.1	4923949	4.03593E-05	**344**	584378.8	4926139	9.49925E-06
300	598843.2	4923049	2.03973E-05	**345**	584385.9	4924978	4.48117E-05
301	599924	4923054	3.57825E-05	**346**	584938.9	4924556	2.53934E-05
302	600815.1	4923066	1.29011E-05	**347**	585989.6	4924514	1.50723E-05
303	601780.5	4923077	2.53832E-05	**348**	585989.3	4923736	1.67248E-05
304	602016.3	4922253	8.14158E-07	**349**	585991.8	4922740	2.41543E-05
305	602746.9	4922189	4.30121E-05	**350**	586004	4921818	2.29505E-06
306	613968.8	4921789	4.19224E-05	**351**	586421.7	4921331	2.96992E-05
307	614325.4	4922410	3.77629E-06	**352**	587434	4921317	2.12459E-05
308	606733	4918716	7.84547E-06	**353**	588391.4	4921345	7.19704E-05
309	606763.1	4919715	1.57232E-05	**354**	589204.8	4921236	0.000117936
310	605918.2	4919853	1.32553E-05	**355**	593056.3	4904440	6.94734E-06
311	597989.6	4928113	3.12495E-06	**356**	592097.5	4904332	6.62467E-06
312	597967.7	4929128	3.67718E-05	**357**	591022	4904009	1.71127E-05
313	597169.4	4929608	3.43325E-05	**358**	590051.6	4904546	3.69358E-06
314	595552.4	4929560	3.86539E-05	**359**	590449.1	4905420	4.65921E-06
315	594317	4929544	6.55726E-05	**360**	590736.6	4906172	7.03051E-06

Table 8.1 (Cont'd)

Sample	Easting	Northing	X (mass normalized)	Sample	Easting	Northing	X (mass normalized)
361	590878.5	4907251	6.76669E-06	**390**	571576.8	4911290	1.11431E-05
362	590854.4	4908127	9.5622E-06	**391**	571727.3	4910410	1.58878E-05
363	590952.2	4909028	5.55281E-06	**392**	573196.4	4910330	2.56886E-05
364	591212	4909833	6.51691E-06	**393**	573238.9	4909150	1.0226E-05
365	591668.6	4910730	1.72884E-05	**394**	573656	4908692	1.09841E-05
366	592073.6	4911501	1.21068E-05	**395**	574658.7	4908634	3.66349E-05
367	592595.5	4912178	1.42984E-05	**396**	589089.5	4913261	5.24143E-06
368	596338.3	4915747	1.19035E-05	**397**	587991.3	4913246	1.11252E-05
369	596326.3	4916828	1.08376E-05	**398**	586910.1	4913243	1.71719E-05
370	596330	4917656	2.0541E-05	**399**	585997.2	4913275	1.12111E-05
371	594775	4918061	3.50809E-05	**400**	585997.1	4914291	6.08619E-06
372	593765.1	4918054	2.61911E-05	**401**	585536.8	4914859	4.29352E-05
373	592826.3	4918077	2.35928E-05	**402**	584650.1	4914842	2.41167E-06
374	591906.4	4918090	2.53975E-05	**403**	583738.8	4914871	1.79042E-05
375	590951.6	4918121	3.44333E-05	**404**	582681.7	4914876	9.55434E-06
376	563489.2	4918514	3.69117E-05	**405**	582034.4	4915351	4.09991E-05
377	563507.9	4917552	3.68396E-05	**406**	582030.3	4916310	3.59382E-05
378	563549.1	4916186	4.97305E-05	**407**	582018.6	4917351	9.81364E-07
379	563734.7	4915391	5.17308E-05	**408**	582098.9	4918242	1.92473E-05
380	564670.7	4915393	5.25068E-05	**409**	582014.3	4919273	3.30354E-05
381	565562.7	4915402	6.75789E-06	**410**	581451.8	4919903	2.27241E-05
382	566518.8	4915388	1.75215E-05	**411**	580497.9	4920107	1.69155E-05
383	566737.7	4914623	9.20944E-05	**412**	578798.1	4920348	1.27912E-06
384	567013.5	4913752	1.85482E-05	**413**	579397.3	4921258	2.2693E-05
385	567949.9	4913734	2.04063E-05	**414**	579565.4	4921933	2.37176E-05
386	568968.7	4913713	2.00559E-05	**415**	579578.8	4923010	1.83996E-05
387	569998.5	4913656	3.52275E-05	**416**	579560.8	4923942	4.47597E-05
388	569989.2	4912784	5.25925E-05	**417**	579116.3	4924618	3.85288E-05
389	571585	4911996	5.67441E-05	**418**	578139.2	4924615	4.82989E-05

Highlighted rows with an asterisk indicate samples used for κ-T, magnetic hysteresis, and frequency dependent magnetic susceptibility investigation.

Figure 8.1 All measured magnetic hysteresis plots.

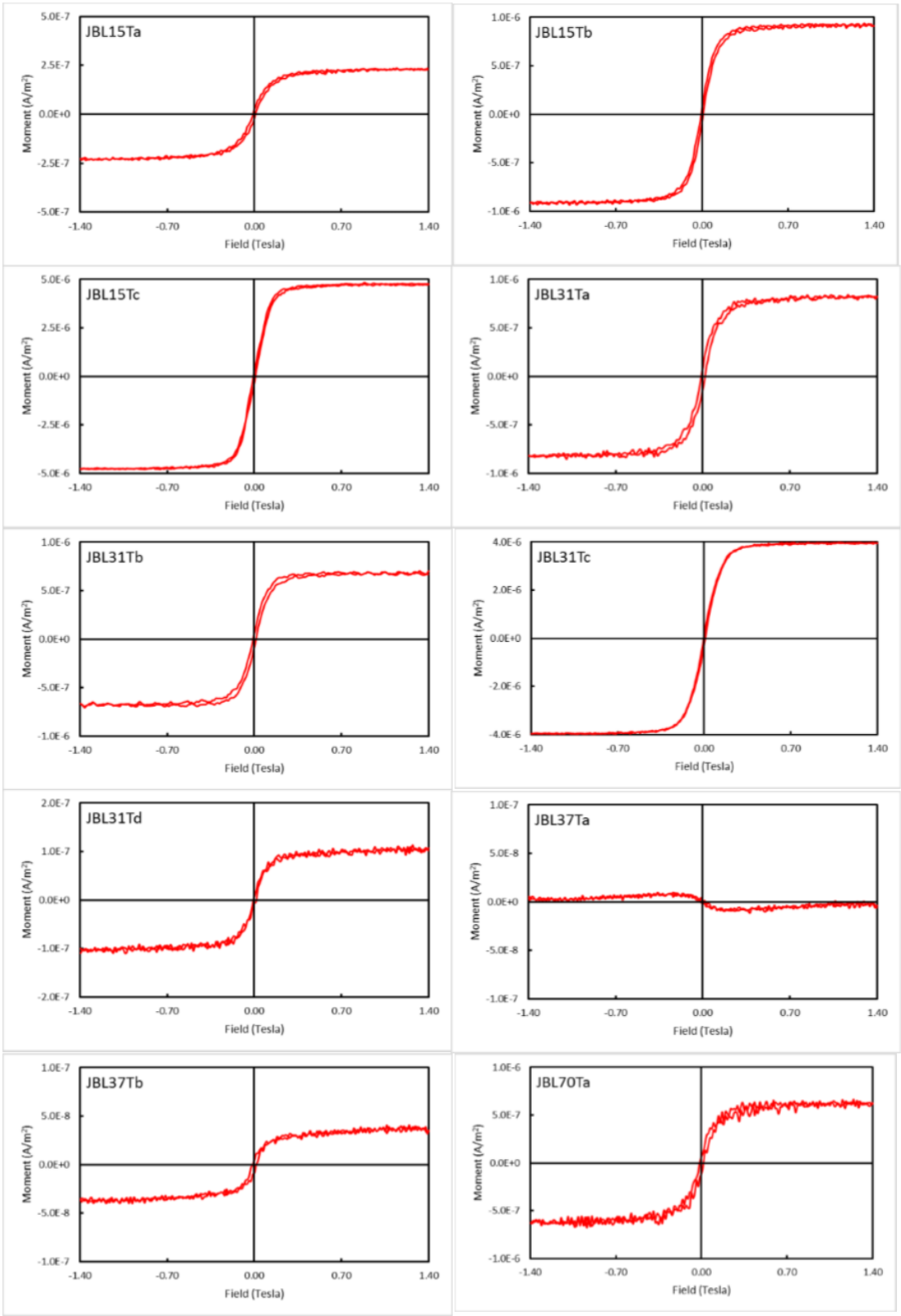

Figure 8.1 (Cont'd)

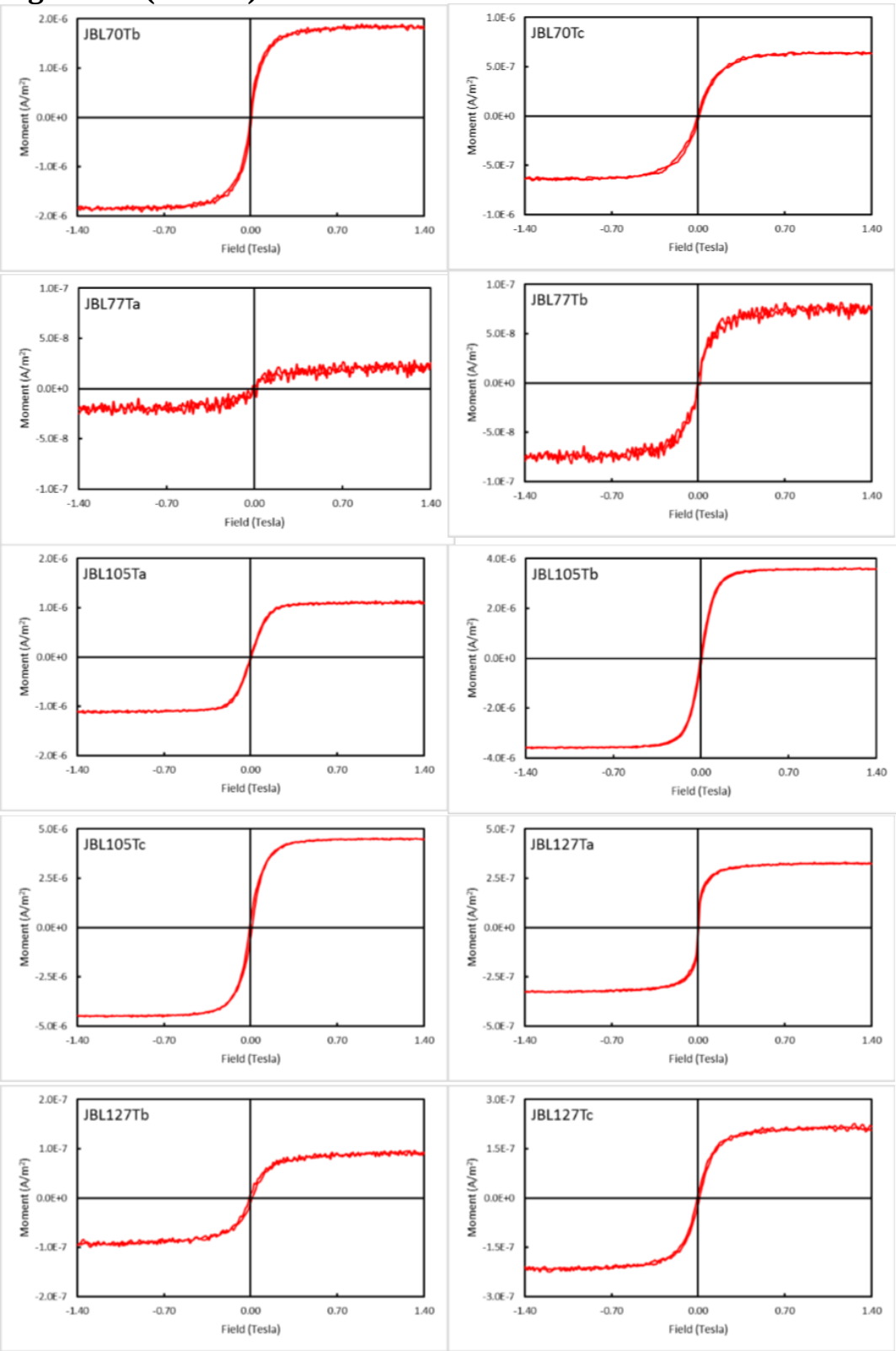

Figure 8.1 (Cont'd)

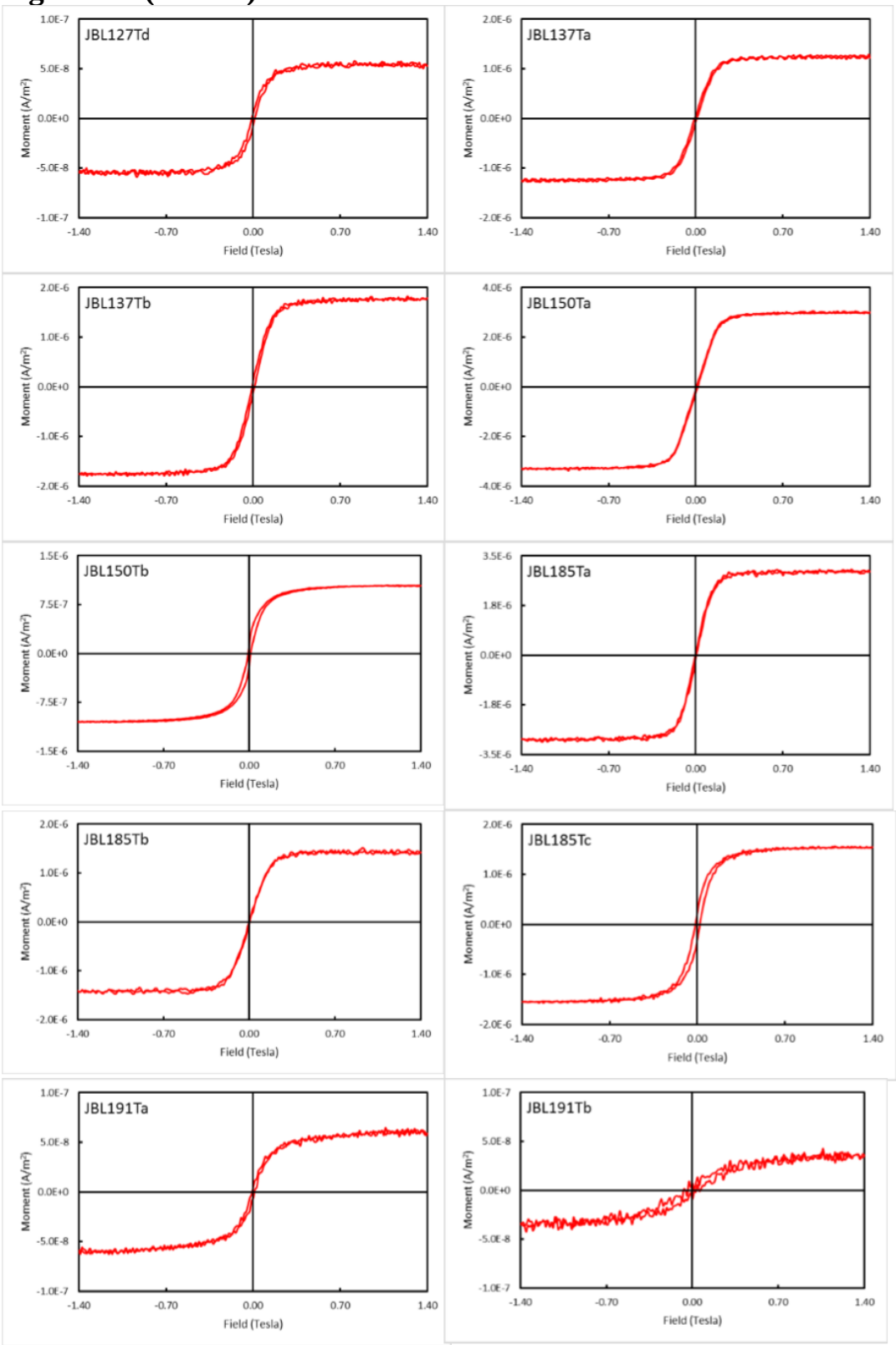

Figure 8.1 (Cont'd)

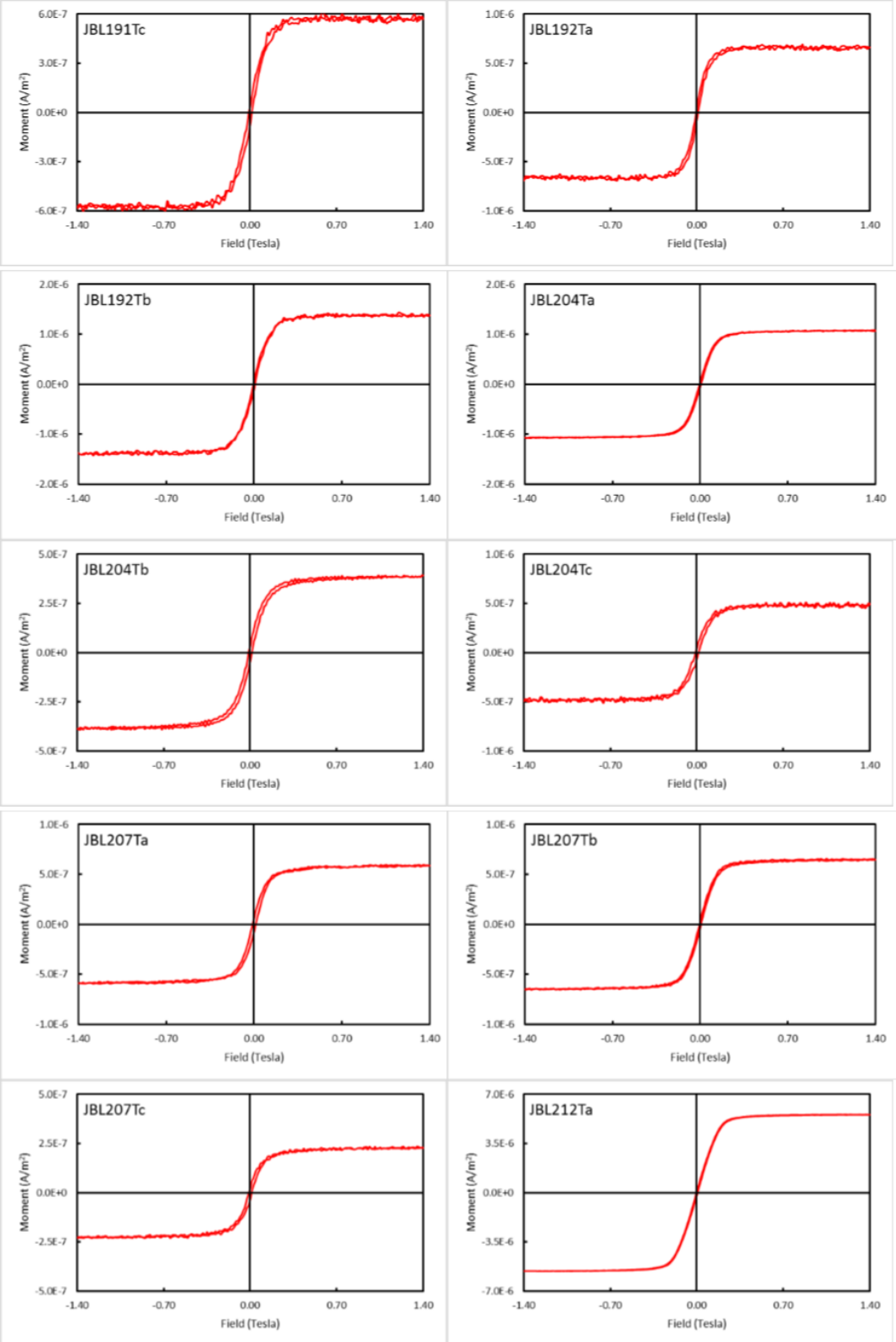

Figure 8.1 (Cont'd)